Intercalated cell depletion and vacuolar H+-ATPase mistargeting in an AE1 R607H knockin model

Mumtaz, Rizwan ; Trepiccione, Francesco ; Hennings, J Christopher ; Huebner, Antje K ; Serbin, Bettina ; Picard, Nicolas ; Ullah, A K M Shahid ; Păunescu, Teodor G ; Capen, Diane E ; Lashhab, Rawad M ; Mouro-Chanteloup, Isabelle ; Alper, Seth L ; Wagner, Carsten A ; Cordat, Emmanuelle ; Brown, Dennis ; Eladari, Dominique ; Hübner, Christian A

Abstract: Distal nephron acid secretion is mediated by highly specialized type A intercalated cells (A-ICs), which contain vacuolar H(+)-ATPase (V-type ATPase)-rich vesicles that fuse with the apical plasma membrane on demand. Intracellular bicarbonate generated by luminal H(+) secretion is removed by the basolateral anion-exchanger AE1. Chronically reduced renal acid excretion in distal renal tubular acidosis (dRTA) may lead to nephrocalcinosis and renal failure. Studies in MDCK monolayers led to the proposal of a dominant-negative trafficking mechanism to explain AE1-associated dominant dRTA. To test this hypothesis in vivo, we generated an Ae1 R607H knockin mouse, which corresponds to the most common dominant dRTA mutation in human AE1, R589H. Compared with wild-type mice, heterozygous and homozygous R607H knockin mice displayed incomplete dRTA characterized by compensatory upregulation of the Na(+)/HCO3(-) cotransporter NBCn1. Red blood cell Ae1-mediated anion-exchange activity and surface polypeptide expression did not change. Mutant mice expressed far less Ae1 in A-ICs, but basolateral targeting of the mutant protein was preserved. Notably, mutant mice also exhibited reduced expression of V-type ATPase and compromised targeting of this proton pump to the plasma membrane upon acid challenge. Accumulation of p62- and ubiquitin-positive material in A-ICs of knockin mice suggested a defect in the degradative pathway, which may explain the observed loss of A-ICs. R607H knockin did not affect type B intercalated cells. We propose that reduced basolateral anion-exchange activity in A-ICs inhibits trafficking and regulation of V-type ATPase, compromising luminal H(+) secretion and possibly lysosomal acidification.

DOI: https://doi.org/10.1681/ASN.2016020169

DOI: https://doi.org/10.1681/ASN.2016020169

Intercalated cell depletion and V-ATPase mistargeting in AE1 R607H knock-in mice

Authors:
Mumtaz R[1,*], Trepiccione F[2,3*], Hennings JC[1,*], Huebner AK[1,*], Serbin B[2,*], Picard N[4], Ullah SA[5], Păunescu TG[6], Capen DE[6], Lashhab RM[5], Mouro-Chanteloup I[7], Alper SL[8], Wagner CA[9], Cordat E[5], Brown D[6], Eladari D[2,*], Hübner CA[1,*]

Affiliations:
[1]Institute of Human Genetics, Jena University Hospital, Friedrich Schiller Universität, Jena, Germany
[2]Institut National de la Santé et de la Recherche Médicale (INSERM) U970, Paris Cardiovascular Research Center and Université Paris Descartes, Department of Physiology, Hopital Européen Georges Pompidou, Paris, France
[3]Department of Cardio-Thoracic and Respiratory Science, Second University of Naples, Naples, Italy
[4]Centre National de la Recherche Scientifique (CNRS) Équipe de Recherche Labellisée (ERL) 8228, Institut National de la Santé et de la Recherche Médicale (INSERM) Unité Mixte de Recherche en Santé (UMR-S) 1138, Université Pierre et Marie Curie, Centre de Recherche des Cordeliers, 15 rue de l'Ecole de Médecine, Paris, France
[5]Department of Physiology, University of Alberta, Edmonton, Alberta, Canada
[6]Center for Systems Biology, Program in Membrane Biology and Division of Nephrology, Massachusetts General Hospital and Department of Medicine, Harvard Medical School, Boston, MA, USA
[7]Institut National de la Transfusion Sanguine; Institut National de la Santé et de la Recherche Médicale (INSERM), Unité Mixte de Recherche en Santé (UMR-S) 1134, Université Paris Diderot and Laboratory of Excellence Globule Rouge-Excellence (GR-Ex), Paris, France
[8]Nephrology Division and Vascular Biology Research Center, Beth Israel Deaconess Medical Center and Department of Medicine, Harvard Medical School, Boston, MA, USA
[9]Institute of Physiology, University of Zurich, Zurich, Switzerland

Correspondence:

Dominique Eladari
INSERM U970, Paris Cardiovascular Research Center, 56 rue Leblanc, F-75015, Paris, France
Dominique.eladari@inserm.fr

Christian A. Hübner
Institute of Human Genetics, Jena University Hospital, Friedrich-Schiller-University Jena, Kollegiengasse 10, 07743 Jena, Germany
Christian.huebner@med.uni-jena.de

[*]equal contribution

Running title: AE1 R607H knock-in mice

Summary

Distal nephron acid secretion is mediated by highly specialized type A intercalated cells (A-ICs), which contain V-type ATPase-rich vesicles that fuse with apical plasma membrane upon demand. Intracellular bicarbonate generated by luminal H^+ secretion is removed by the basolateral anion-exchanger AE1. Chronically reduced renal acid excretion of distal renal tubular acidosis (dRTA) may lead to nephrocalcinosis and renal failure. A dominant-negative trafficking mechanism was proposed to explain AE1-associated dominant dRTA based on unequivocal studies in MDCK monolayers. To test this hypothesis in vivo, we have generated a R607H knock-in mouse, which corresponds to the most common dominant dRTA mutation in human AE1, R589H. Heterozygous and homozygous R607H knock-in mice only displayed incomplete dRTA paralleled by the compensatory upregulation of the Na^+/HCO_3^- cotransporter NBCn1. Red blood cell Ae1-mediated anion-exchange activity and surface polypeptide expression were unchanged. Ae1 expression in A-ICs was greatly reduced, but basolateral targeting of the mutant protein was preserved. Unexpectedly, V-type ATPase expression was also reduced, and its plasma membrane targeting upon acid challenge compromised. Accumulation of p62- and Ubiquitin-positive material in A-ICs of knock-in mice suggested a defect in the degradative pathway, which may ultimately lead to loss of A-ICs. Type B intercalated cells were unaffected. We propose that reduced basolateral anion-exchange activity in A-ICs inhibits trafficking and regulation of V-type ATPase, compromising luminal H^+ secretion and possibly also lysosomal acidification.
(223 words)

Introduction

The kidney plays a major role in acid-base homeostasis. Renal acidification defects do not necessarily result in overt systemic metabolic acidosis, but often lead to growth retardation, hypokalemia, osteomalacia, and hypercalciuria, with potential complications of nephrolithiasis or nephrocalcinosis [1].

Net elimination of non-volatile acid is mediated by type A-intercalated cells (A-ICs) in the connecting tubule (CNT) and collecting duct (CD). To achieve proton (H^+) secretion, A-ICs express V-type ATPase at the apical cell pole [2]. Protons are generated within these cells by hydration of CO_2, which is ~~a~~ catalyzed by intracellular carbonic anhydrase type II (CAII). The resulting H_2CO_3 dissociates into H^+ and HCO_3^-. While H^+ is secreted apically via proton pumps, HCO_3^- is extruded basolaterally by the chloride/bicarbonate exchanger AE1 (SLC4A1). This transport model is supported by hereditary defects, also known as distal renal tubular acidosis (dRTA), caused by mutations of proton pump subunits a4 or B1, of carbonic anhydrase CA II, or of anion-exchanger AE1, respectively [1, 3].

The *SLC4A1* gene encodes two transcripts encoding erythroid variant eAE1 and N-terminally truncated kidney variant kAE1. Global disruption of both variants in mice causes life-threatening hemolytic anemia and dRTA, whereas heterozygous knock-out mice are grossly normal [4, 5]. In humans, AE1 mutations can cause dRTA of either autosomal recessive or dominant type. Whereas most recessive forms of dRTA present early with nephrolithiasis, nephrocalcinosis and hemolytic anemia, dominant forms are usually diagnosed later in life and only rarely develop clinically apparent hemolytic anemia [6]. The most common dominant variant, AE1 R589H, was shown to exhibit only mild reduction in anion-exchange activity [6]. Retention of heterologous AE1 R589H in the endoplasmic reticulum of polarized MDCK cells, along with co-retention of co-expressed wild-type AE1, supported the hypothesis that dominant negative trafficking defects underlie autosomal dominant dRTA caused by heterozygous AE1 mutations [7].

To test this hypothesis *in vivo,* we generated mice expressing the variant R607H, corresponding to human variant R589H. Both heterozygous and homozygous knock-in mice exhibited incomplete dRTA, less severe in heterozygotes than in homozygotes. Targeting of Ae1 R607H to the basolateral plasma membrane of A-ICs was unexpectedly normal, as was transport activity *in vivo*. We further found that impaired targeting of the V-type ATPase and a decreased number of A-ICs underlie impaired acid secretion in both heterozygous and homozygous knock-in mice.

Results:

Generation of Ae1 R607H knock-in mice

We introduced the orthologous mouse Ae1 mutation R607H into murine embryonic stem (ES) cells by homologous recombination. The R607H mutation is located within transmembrane span 6 near its cytoplasmic end [8] (Figure 1A,B). Homologous recombination was verified by Southern blot analysis exploiting the *Hind*III restriction site within intron 14 (Supplementary Figure 1A,B) and by sequence analysis (Figure 1C). Heterozygous and homozygous knock-in mice were viable and appeared grossly normal. Bodyweight did not differ between genotypes (Table 1).

As observed in human dRTA patients heterozygous for AE1 R589H, R607H knock-in red blood cell counts and morphology were unaffected (Figure 1D and Table 1). Neither Masson-Goldner stain of kidney sections revealed gross structural abnormalities (Supplementary Figure 1C), nor Von Kossa stain revealed nephrocalcinosis or nephrolithiasis by age 3 months (Supplementary Figure 1D).

Heterozygous and homozygous R607H knock-in mice display incomplete dRTA

Although knock-in mice excreted urine that was more alkaline than that of their wild-type littermates, acid-base status and renal net acid excretion were comparable in all genotypes under baseline conditions (Table 1).

As typical for renal acidosis plasma chloride levels were increased, while plasma [HCO_3^-], pH and pCO_2, which can change with respiration and are less robust, appeared unchanged. Interestingly, homozygous knock-in mice showed hypocalciuria, which is supported by the observation that increased urine pH may be associated with lower calcium excretion [9], although the mechanism remains unclear.

We next challenged male *Ae1*$^{+/R607H}$, *Ae1*$^{R607H/R607H}$ and wild-type littermates with 0.28 M NH_4Cl in drinking water. All groups developed metabolic acidosis in response to NH_4Cl administration, with decreased blood pH (Figure 1E) and plasma [HCO_3^-] (Supplementary Figure 2A), associated with increased blood [Cl^-] (Figure 1F).

During acid load, blood pCO_2 was decreased independent of genotype, indicating respiratory adaptation (Supplementary Figure 2B). Urine pH decreased upon acute acid challenge. Only in wild-type mice blood pH (Figure 1E) recovered to baseline and urine pH remained low during sustained acid loading (Figure 1G) due to increased net acid (Supplementary Figure 2C), NH_4^+ (Figure 1H) and titratable acid excretion (Supplementary Figure 2D). Homozygous knock-in mice exhibited a more marked renal acidification defect and were completely unable to recover from the acid load, developing persistent post-treatment metabolic acidosis with reduced body weight secondary to reduced water and food intake (Supplementary Figure 2E-G).

These data demonstrate incomplete dRTA in knock-in mice, a phenotype compatible with, but of lesser apparent severity than that of dRTA patients heterozygous for AE1 R589H [6]. To exclude compensatory mechanisms in knock-in mice, we tested the expression of several acid/base transport proteins. We found no differences in NBC1 (Slc4a4), NHE3 (Slc9a3), AE2 (Slc4a2) or H^+/K^+-ATPase subunit expression, but NBCn1 (Slc4a7), proposed to favor NH_4^+ secretion in the collecting duct [10], was strongly upregulated (Figure 2A-C).

The R607H/R589H kAE1 variant is correctly targeted to the basolateral plasma membrane of A-ICs.

As in wild-type mice (Figure 3A,D), the kAe1 signal was clearly localized to the basolateral membrane in kidney sections of *Ae1*$^{R607H/R607H}$ mice (Figure 3C,F and Supplementary Figure 3) indicating that normal targeting of the mutant polypeptide is preserved in both cortex and medulla. A typical basolateral signal was also obtained in *Ae1*$^{+/R607H}$ mice (Figure 3B,E and Supplementary Figure 3). The immunolabeling intensity, however, appeared less pronounced in *Ae1*$^{+/R607H}$ and *Ae1*$^{R607H/R607H}$ mice.

Ultrastructural analysis of immunogold-labeled kAe1 further supports normal targeting of the R607H variant to the basolateral plasma membrane (Figure 3G-I), but with lower labeling intensity than in WT mice.

These unexpected localization prompted examination of human kAE1 R589H targeting in M-1 cells (Figure 3J,K and Supplementary Figure 3), derived from mouse cortical collecting duct, and in mIMCD-3 cells (Figure 3L,M and

Supplementary Figure 3), derived from mouse inner medullary collecting duct. In both cell models, targeting of kAE1 to the basolateral plasma membrane was unaffected by the mutation.

These results, therefore, differ from those repeatedly observed in polarized MDCK cell monolayers, and thus argue against the prevailing concept that trafficking or targeting defects underlie human autosomal dominant dRTA caused by the AE1 R589H mutation.

The R607H/R589H mutation does not impair Ae1-dependent chloride-bicarbonate exchange activity *in vitro* and *in vivo*

Cl^-/HCO_3^- exchange activity in IMCD-3 cells transfected with either wild-type kAE1, kAE1 R589H, or both was stimulated to similar extents upon extracellular Cl^- removal (Figure 4A,B), suggesting that the R589H variant does not impair Cl^-/HCO_3^- exchange activity. Stopped-flow fluorimetry measurements (10) of Cl^--dependent HCO_3^- influx in resealed red blood cell ghosts similarly showed no difference in anion-exchange activity among genotypes (Figure 4C,D). Moreover, surface abundance of red cell eAe1 as assessed by FACS (Figure 4E,F) and total red cell eAe1 content (Supplementary Figure 4) in mutant mice were indistinguishable from corresponding values measured in wild-type red cells.

kAe1 expression is reduced in the kidney of *Ae1*$^{+/R607H}$ and *Ae1*$^{R607H/R607H}$ mice

Ae1 transcript abundance was reduced both in the cortex (Figure 5A) and in the medulla of *Ae1*$^{+/R607H}$ and *Ae1*$^{R607H/R607H}$ mice (Figure 5B), likely either reflecting decreased transcriptional efficiency, increased transcript degradation and/or decreased A-IC numbers.

In accordance, kAe1 protein levels were strongly reduced in cortical and medullary lysates from both *Ae1*$^{+/R607H}$ and *Ae1*$^{R607H/R607H}$ mice (Figure 5C-D and Supplementary Figure 5). Ae1 immunostaining revealed not only decreased fluorescence intensity in individual cells, but also reduced numbers of kAe1-positive cells (Figure 5E). This decreased kAe1 immunoreactivity could reflect decreased protein stability of the R607H variant in intercalated cells. However, the ~24 h half-life of recombinant human kAE1 R589H-HA as

measured by pulse-chase experiments in both M1 cells (Figure 5F) and mIMCD-3 cells (Figure 5G) was indistinguishable from that of wild-type human kAE1-HA (See Supplementary Figure 6 for original immunoblots). These results resembled half-lives of the human wild-type and mutant proteins in HEK-293 cells [11] but differed greatly from the kAE1-R598H half-life of 1-2 hours measured in polarized MDCK monolayers [7, 12].

Although anion transport activities of mouse kAE1 R607H and human kAE1 R589H are unchanged, the strongly decreased expression levels suggest that basolateral anion-exchange activity is severely compromised in renal A-ICs of *Ae1*$^{+/R607H}$ and *Ae1*$^{R607H/R607H}$ mice.

Apical sorting of the proton pump is compromised in *Ae1*$^{+/R607H}$ and *Ae1*$^{R607H/R607H}$ mice

Since intercalated cell kAE1 and V-type ATPase are functionally coupled, we assessed targeting of the V-type ATPase B1 subunit in mice at baseline (Supplementary Figure 7) and after acid challenge (Figure 6 and Supplementary Figure 8). After acid challenge the B1 subunit localized almost exclusively to the apical domain of A-ICs in WT mice (Figure 6A). However, in *Ae1*$^{+/R607H}$ (Figure 6B) and *Ae1*$^{R607H/R607H}$ (Figure 6C) mice this apical localization was severely compromised, suggesting altered proton pump targeting.

Immunogold labeling of the A subunit of the V-type ATPase under baseline conditions confirmed decreased labeling of intracellular vesicles at the apical pole of A-ICs (Figure 6G-I). In contrast, V-ATPase labeling was preserved in B-ICs and overall Pendrin expression did not differ (Supplementary Figure 9). Total renal cortical B1 subunit abundance was decreased in acid-challenged mice as judged by cortical membrane fraction immunoblot (Figure 6J).

The Ae1 R607H mutation causes a marked depletion of A-ICs, potentially caused by defective autophagy

We co-stained kidney sections for Ae1, Pendrin, and the E-subunit of the V-type ATPase in wild-type and mutant mice (Figure 7A and Supplementary Figure 10). Importantly, all Pendrin-negative cells that stained for the E-subunit, i.e. A-ICs, also expressed Ae1. Conversely, Pendrin-positive cells B-

ICs never co-stained with Ae1. In a separate experiment we also co-stained for Ae1, Pendrin, and Aquaporin 2 to identify principal cells (Figure 7B and Supplementary Figure 11). While the number of A-ICs was dramatically reduced in the cortex of both *Ae1*$^{+/R607H}$ and *Ae1*$^{R607H/R607H}$ mice, the number of B-ICs and principal cells remained unchanged. Therefore, the proportion of type A-to-B intercalated cells was significantly decreased (Figure 7C). This effect was even more pronounced after the acid challenge (Figure 7D).

We also estimated the size of A-ICs by measuring the section area of individual A-ICs as described previously [13]. A-ICs were larger in heterozygous and homozygous knock-in mice (Figure 7E).

Ultrastructural analysis of A-ICs revealed that the typical intracellular vesicles observed in A-ICs of wild-type mice (Figure 8A,D,G) were depleted in *Ae1*$^{+/R607H}$ (Figure 8B,E,H) and *Ae1*$^{R607H/R607H}$ mice (Figure 8C,F,I). In contrast, the A-ICs of *Ae1*$^{+/R607H}$ and *Ae1*$^{R607H/R607H}$ mice contained numerous atypical lysosome-like vesicles reminiscent of autophagic structures (Figure 8B,C,E,F,H,I) and multilamellar bodies (Figure 8I).

In cortical (Figure 8J-L, Supplementary Figure 12) and medullary (Supplementary Figure 13) A-ICs in *Ae1*$^{+/R607H}$ and *Ae1*$^{R607H/R607H}$ mice co-staining with p62, a receptor for intracellular toxic waste destined for autophagy [14], further supported the interpretation of autophagic vesicles. Importantly, these vesicular structures also partially co-localized with Ubiquitin (Figure 8M-O and Supplementary Figure 14), which marks proteins for degradation [15].

Discussion

Mice genetically lacking Ae1 exhibited severe dRTA characterized by metabolic acidosis in nephrocalcinosis associated with hypercalciuria, hyperphosphaturia, and hypocitraturia, whereas heterozygous knock-out mice were unaffected [4]. However, Ae1-deficient mice are also characterized by high peri- and postnatal lethality, most likely attributable to severe hemolytic anemia. The severe anemia and renal medullary hypoxia, accompanied by elevated levels of toxic free hemoglobin and pathological hemosiderosis all likely contribute to aggravation of the intrinsic defect in renal acid excretion. Indeed, sickle cell disease patients with hemolytic anemia and renal medullary ischemia often develop metabolic acidosis as part of sickle nephropathy [16].

To study the role of Ae1 in the kidney independent of the red blood cell phenotype, we modeled the most common AE1 mutation found in dominant dRTA patients, AE1 R589H, in mice. *Ae1*$^{R607H/+}$ mice were unable to maximally decrease urine pH or to increase urinary excretion of ammonium and titratable acid in response to acid as compared to wild-type. Homozygous knock-in mice were completely unable to recover from an acid load, developing a persistent metabolic acidosis following this challenge.

The phenotype of R607H mice is mild compared to the usually complete dRTA observed in humans with the R589H mutation, although considerable variability of clinical presentation can be observed among affected individuals even within a family. One possible explanation is diet, as the standard mouse chow provides a large net dietary alkali load [17], whereas the typical Western human diet constitutes a net acid load. Species-specific differences should also be considered, as these have been noted in other models, including the V-ATPase B1 subunit (Atp6v1b1) knock-out mouse generated in a mixed SVJ129/C57BL/6 background similar to that of our present study [18]. Different to humans, mice may also have a compensatory upregulation of other transporters, since Ae1 disruption reduced Cl^-/HCO_3^- exchange in isolated outer medullary collecting duct by only 60 % [4]. We here identified NBCn1 to be upregulated in heterozygous and even more so in homozygous knock-in mice. Since NBCn1 is a basolateral Na^+/HCO_3^- cotransporter of the medullary TAL, which was proposed to support NH_4^+/NH_3 excretion in chronic metabolic

acidosis [10], this upregulation may contribute to the mild phenotype of *Ae1*$^{R607H/+}$ and *Ae1*$^{R607H/+}$ mice.

While a dominant or co-dominant mis-targeting to the apical membrane was reported for a C-terminal truncation variant [19, 20], the kAE1 R589H variant exhibited a dominant negative intracellular retention phenotype in confluent polarized MDCK cells [7] as well as in nonpolarized HEK-293 cells [11]. In stark contrast to results in MDCK cells basolateral Ae1 localization was preserved in heterozygous Ae1 R607H knock-in mice as judged by immunofluorescence and immunogold electron microscopy. Even in homozygous knock-in mice, mutant Ae1 localized at the basolateral membrane without accumulation in a cytoplasmic compartment, strongly suggesting normal targeting of the pathological R607H variant. Analysis in the cortical collecting duct cell line M1 and in the medullary collecting duct cell line mIMCD-3 also revealed a predominant basolateral localization of the HA-tagged R589H variant.

Previous studies reported that recombinant kAE1 R589H expressed in *Xenopus* oocytes showed a 20-50 % reduction in Cl^-/Cl^- and Cl^-/HCO_3^- exchange activity and did not display a dominant negative phenotype for anion transport when co-expressed with wild-type kAE1 [6]. Our stopped-flow fluorimetric measurements of Cl^--dependent HCO_3^- influx in resealed red cell ghosts revealed no genotype-dependent difference in transport activity. Transport activity was also unchanged in IMCD-3 cells transfected with the R589H variant.

In remarkable contrast to the red blood cell, Ae1 expression in the kidney was strongly reduced. This observation is in line with a previous observation reporting strong reduction or absence of AE1 staining in renal cortex from a dRTA patient heterozygous for AE1 R589H [21]. Thus basolateral bicarbonate efflux from renal A-ICs can be assumed to be reduced in correlation with the number of *Ae1* alleles affected by the mutation.

Acid secretion in *Ae1*$^{+/R607H}$ and *Ae1*$^{R607H/R607H}$ mice is further compromised by reduced plasma membrane abundance of V-type ATPase possibly reflecting a trafficking defect. This was particularly prominent in mice subjected to an acid challenge normally associated with massive translocation of the multimeric

pump from intracellular compartments to the apical plasma membrane of A-ICs [2]. Instead of the regular V-type ATPase positive vesicles we observed atypical vesicular structures, reminiscent of cell vacuolation in A-ICs of knockin mice, which can occur in response to different types of stress [22]. Notably, the accumulation of intracellular p62- and Ubiquitin-positive structures in A-ICs of *Ae1*$^{+/R607H}$ and *Ae1*$^{R607H/R607H}$ mice suggests a defect in the degradative pathway and/or in autophagy [23], which may be related to defective lysosomal targeting of the V-type ATPase. Notably, impaired V-ATPase activity due to inactivation of the renal (pro)renin receptor also resulted in multilamellar bodies and defects in autophagy [24].

The mechanism by which kAe1 R607H severely perturbs V-type ATPase targeting in the absence of known physical association or subcellular colocalization remains unclear. Since impaired basolateral HCO_3^- extrusion should alkalinize A-ICs, the pH dependence of microtubule assembly [25], actin polymerization/depolymerization [26-29], and other cytoskeletal dynamics may well contribute to the targeting defect. A similar mechanism has been proposed in a murine model of osteopetrosis for altered V-ATPase targeting in osteoclasts deficient in the basolateral anion-exchanger Ae2 [30]. In the kidney, microtubule disruption has dramatic effects on the polarized distribution of several important membrane proteins including the V-type-ATPase [31].

Taken together, the data suggest that the R607H variant (and by extension, the R589H variant in humans) may disrupt the normal trafficking of V-type ATPase to the plasma membrane and lysosomes in A-ICs. The latter may explain accumulation of p62/Ubiquitin-positive structures, perhaps eventuating in the decreased total number of A-ICs, which perpetuates the acid secretion defect. These findings illustrate the considerable, context-dependent complexity of AE1-related kidney disease.

Concise methods

All animal experiments were approved by the Thüringer Landesamt für Lebensmittelsicherheit und Verbraucherschutz (TLLV) in Germany.

Generation of Ae1-R607H mice and metabolic parameters

The generation of Ae1-R607H mice is described in the supplemental information. Urine was collected daily under mineral oil after adjustment to metabolic cages (Tecniplast, Buguggiate, Italy). Urine pH was measured with a microelectrode (InLab Micro pH, Mettler Toledo, Viroflay, France). Retro-orbital blood was analyzed with the ABL 77 pH/blood-gas analyser (Radiometer, Copenhagen, Denmark).

Immunohistochemistry and electron microscopy

Kidneys were fixed by retrograde perfusion of the aorta with 4 % PFA in phosphate buffer and flash frozen in isopentane cooled with liquid nitrogen. The staining procedure and relevant antibodies are listed in the supplemental information. For electron microscopy tissues were further fixed in 2 % glutaraldehyde in 0.1 M sodium cacodylate pH 7.4 (Electron Microscopy Sciences, Hatfield, PA, USA) and subsequently treated with osmium tetroxide (Electron Microscopy Sciences). Ultrathin sections were stained with lead citrate and uranyl acetate and in a JEOL 1011 transmission electron microscope (TEM; JEOL, Peabody, MA, USA).

Immunoblotting

Kidneys were placed in ice-cold PBS, homogenized and membrane-enriched fractions were prepared by centrifugation. Proteins were separated by SDS-PAGE and blotted onto a nitrocellulose membrane. Membranes were incubated with the respective antibodies for immunodetection with Pierce ECL Western Blotting Substrate (Thermo Scientific, Waltham, MA, USA), and analyzed by LAS 4000 ImageQuant (GE Healthcare, Little Chalfont, UK).

Detailed methods are listed in the supplemental information.

Acknowledgements

We are grateful to Katrin Schorr and Denis Arutyunov for excellent experimental support. We are indebted to Thomas D. DuBose Jr. for providing the H^+/K^+-ATPase antibodies. This study was funded by the DFG (Hu 800/8-1) and the Else-Kröner-Fresenius-Stiftung to CAH; a fellowship by the IZKF Jena to JCH, the Canadian Institutes of Health Research (MOP142251) and the Kidney Foundation of Canada to EC; the International Research Training Group in Membrane Biology from the NSERC-CREATE 414205-2012 program to RML and SAU; the Swiss National Science Foundation ((31003A_155959/1) to CAW; the NIH (DK042956) and the Boston Area Diabetes and Endocrinology Research Center (DK57521) and the MGH Center for the Study of Inflammatory Bowel Disease (DK43351) supporting the Program in Membrane Biology Microscopy Core facility to DB, TGP and DEC; the ERA-EDTA LTF41-2013 to FT; the l'Agence Nationale de la Recherche (ANR) ANR BLANC 14-CE12-0013-01/HYPERSCREEN, the grants ECOS/CONYCIT France-Chile 2014 and CHLORBLOCK from the IDEX Sorbonne Paris Cité to DE; a fellowship from the CONYCIT to KL. NP was supported by the Fondation du Rein, the French Nephrology Society sous égide de la Fondation pour la Recherche Médicale and by ANR grant 15-CE14-0024-02/ConTarKiD.

Statement of competing financial interests

None.

References

1. Batlle, D, Haque, SK: Genetic causes and mechanisms of distal renal tubular acidosis. *Nephrology, dialysis, transplantation : official publication of the European Dialysis and Transplant Association - European Renal Association,* 27**:** 3691-3704, 2012.
2. Wagner, CA, Finberg, KE, Breton, S, Marshansky, V, Brown, D, Geibel, JP: Renal vacuolar H+-ATPase. *Physiological reviews,* 84**:** 1263-1314, 2004.
3. Alper, SL: Familial renal tubular acidosis. *Journal of nephrology,* 23 Suppl 16**:** S57-76, 2010.
4. Stehberger, PA, Shmukler, BE, Stuart-Tilley, AK, Peters, LL, Alper, SL, Wagner, CA: Distal renal tubular acidosis in mice lacking the AE1 (band3) Cl-/HCO3- exchanger (slc4a1). *Journal of the American Society of Nephrology : JASN,* 18**:** 1408-1418, 2007.
5. Akel, A, Wagner, CA, Kovacikova, J, Kasinathan, RS, Kiedaisch, V, Koka, S, Alper, SL, Bernhardt, I, Wieder, T, Huber, SM, Lang, F: Enhanced suicidal death of erythrocytes from gene-targeted mice lacking the Cl-/HCO(3)(-) exchanger AE1. *American journal of physiology Cell physiology,* 292**:** C1759-1767, 2007.
6. Jarolim, P, Shayakul, C, Prabakaran, D, Jiang, L, Stuart-Tilley, A, Rubin, HL, Simova, S, Zavadil, J, Herrin, JT, Brouillette, J, Somers, MJ, Seemanova, E, Brugnara, C, Guay-Woodford, LM, Alper, SL: Autosomal dominant distal renal tubular acidosis is associated in three families with heterozygosity for the R589H mutation in the AE1 (band 3) Cl-/HCO3- exchanger. *The Journal of biological chemistry,* 273**:** 6380-6388, 1998.
7. Cordat, E, Kittanakom, S, Yenchitsomanus, PT, Li, J, Du, K, Lukacs, GL, Reithmeier, RA: Dominant and recessive distal renal tubular acidosis mutations of kidney anion exchanger 1 induce distinct trafficking defects in MDCK cells. *Traffic,* 7**:** 117-128, 2006.
8. Arakawa, T, Kobayashi-Yurugi, T, Alguel, Y, Iwanari, H, Hatae, H, Iwata, M, Abe, Y, Hino, T, Ikeda-Suno, C, Kuma, H, Kang, D, Murata, T, Hamakubo, T, Cameron, AD, Kobayashi, T, Hamasaki, N, Iwata, S: Crystal structure of the anion exchanger domain of human erythrocyte band 3. *Science,* 350**:** 680-684, 2015.
9. Bonny, O, Rubin, A, Huang, CL, Frawley, WH, Pak, CY, Moe, OW: Mechanism of urinary calcium regulation by urinary magnesium and pH. *Journal of the American Society of Nephrology : JASN,* 19**:** 1530-1537, 2008.
10. Kwon, TH, Fulton, C, Wang, W, Kurtz, I, Frokiaer, J, Aalkjaer, C, Nielsen, S: Chronic metabolic acidosis upregulates rat kidney Na-HCO cotransporters NBCn1 and NBC3 but not NBC1. *American journal of physiology Renal physiology,* 282**:** F341-351, 2002.
11. Quilty, JA, Li, J, Reithmeier, RA: Impaired trafficking of distal renal tubular acidosis mutants of the human kidney anion exchanger kAE1. *American journal of physiology Renal physiology,* 282**:** F810-820, 2002.
12. Chu, CY, King, JC, Berrini, M, Alexander, RT, Cordat, E: Functional rescue of a kidney anion exchanger 1 trafficking mutant in renal epithelial cells. *PloS one,* 8**:** e57062, 2013.

13. West, MJ: Estimating volume in biological structures. *Cold Spring Harbor protocols,* 2012**:** 1129-1139, 2012.
14. Komatsu, M, Kurokawa, H, Waguri, S, Taguchi, K, Kobayashi, A, Ichimura, Y, Sou, YS, Ueno, I, Sakamoto, A, Tong, KI, Kim, M, Nishito, Y, Iemura, S, Natsume, T, Ueno, T, Kominami, E, Motohashi, H, Tanaka, K, Yamamoto, M: The selective autophagy substrate p62 activates the stress responsive transcription factor Nrf2 through inactivation of Keap1. *Nature cell biology,* 12**:** 213-223, 2010.
15. Komander, D, Rape, M: The ubiquitin code. *Annual review of biochemistry,* 81**:** 203-229, 2012.
16. Maurel, S, Stankovic Stojanovic, K, Avellino, V, Girshovich, A, Letavernier, E, Grateau, G, Baud, L, Girot, R, Lionnet, F, Haymann, JP: Prevalence and correlates of metabolic acidosis among patients with homozygous sickle cell disease. *Clinical journal of the American Society of Nephrology : CJASN,* 9**:** 648-653, 2014.
17. Lin, SH, Cheema-Dhadli, S, Chayaraks, S, Chen, CB, Gowrishankar, M, Halperin, ML: Physiological disposal of the potential alkali load in diet of the rat: steps to achieve acid-base balance. *The American journal of physiology,* 274**:** F1037-1044, 1998.
18. Finberg, KE, Wagner, CA, Bailey, MA, Paunescu, TG, Breton, S, Brown, D, Giebisch, G, Geibel, JP, Lifton, RP: The B1-subunit of the H(+) ATPase is required for maximal urinary acidification. *Proceedings of the National Academy of Sciences of the United States of America,* 102**:** 13616-13621, 2005.
19. Devonald, MA, Smith, AN, Poon, JP, Ihrke, G, Karet, FE: Non-polarized targeting of AE1 causes autosomal dominant distal renal tubular acidosis. *Nature genetics,* 33**:** 125-127, 2003.
20. Toye, AM, Banting, G, Tanner, MJ: Regions of human kidney anion exchanger 1 (kAE1) required for basolateral targeting of kAE1 in polarised kidney cells: mis-targeting explains dominant renal tubular acidosis (dRTA). *Journal of cell science,* 117**:** 1399-1410, 2004.
21. Shayakul, C, Jarolim, P, Zachlederova, M, Prabakaran, D, Cortez-Campeao, D, Kalabova, D, Stuart-Tilley, AK, Ideguchi, H, Haller, C, Alper, SL: Characterization of a highly polymorphic marker adjacent to the SLC4A1 gene and of kidney immunostaining in a family with distal renal tubular acidosis. *Nephrology, dialysis, transplantation : official publication of the European Dialysis and Transplant Association - European Renal Association,* 19**:** 371-379, 2004.
22. Merski, JA, Meyers, MC: Light- and electron-microscopic evaluation of renal tubular cell vacuolation induced by administration of nitrilotriacetate or sucrose. *Food and chemical toxicology : an international journal published for the British Industrial Biological Research Association,* 23**:** 923-930, 1985.
23. Komatsu, M, Waguri, S, Koike, M, Sou, YS, Ueno, T, Hara, T, Mizushima, N, Iwata, J, Ezaki, J, Murata, S, Hamazaki, J, Nishito, Y, Iemura, S, Natsume, T, Yanagawa, T, Uwayama, J, Warabi, E, Yoshida, H, Ishii, T, Kobayashi, A, Yamamoto, M, Yue, Z, Uchiyama, Y, Kominami, E, Tanaka, K: Homeostatic levels of p62 control cytoplasmic inclusion body formation in autophagy-deficient mice. *Cell,* 131**:** 1149-1163, 2007.

24. Trepiccione, F, Gerber, SD, Grahammer, F, Lopez-Cayuqueo, KI, Baudrie, V, Paunescu, TG, Capen, DE, Picard, N, Alexander, RT, Huber, TB, Chambrey, R, Brown, D, Houillier, P, Eladari, D, Simons, M: Renal Atp6ap2/(Pro)renin Receptor Is Required for Normal Vacuolar H+-ATPase Function but Not for the Renin-Angiotensin System. *Journal of the American Society of Nephrology : JASN*, 2016.
25. Regula, CS, Pfeiffer, JR, Berlin, RD: Microtubule assembly and disassembly at alkaline pH. *The Journal of cell biology,* 89**:** 45-53, 1981.
26. Wang, F, Sampogna, RV, Ware, BR: pH dependence of actin self-assembly. *Biophysical journal,* 55**:** 293-298, 1989.
27. Hawkins, M, Pope, B, Maciver, SK, Weeds, AG: Human actin depolymerizing factor mediates a pH-sensitive destruction of actin filaments. *Biochemistry,* 32**:** 9985-9993, 1993.
28. Yonezawa, N, Nishida, E, Sakai, H: pH control of actin polymerization by cofilin. *The Journal of biological chemistry,* 260**:** 14410-14412, 1985.
29. Bernstein, BW, Painter, WB, Chen, H, Minamide, LS, Abe, H, Bamburg, JR: Intracellular pH modulation of ADF/cofilin proteins. *Cell motility and the cytoskeleton,* 47**:** 319-336, 2000.
30. Coury, F, Zenger, S, Stewart, AK, Stephens, S, Neff, L, Tsang, K, Shull, GE, Alper, SL, Baron, R, Aliprantis, AO: SLC4A2-mediated Cl-/HCO3- exchange activity is essential for calpain-dependent regulation of the actin cytoskeleton in osteoclasts. *Proceedings of the National Academy of Sciences of the United States of America,* 110**:** 2163-2168, 2013.
31. Brown, D, Sabolic, I, Gluck, S: Colchicine-induced redistribution of proton pumps in kidney epithelial cells. *Kidney international Supplement,* 33**:** S79-83, 1991.
32. Barneaud-Rocca, D, Etchebest, C, Guizouarn, H: Structural model of the anion exchanger 1 (SLC4A1) and identification of transmembrane segments forming the transport site. *The Journal of biological chemistry,* 288**:** 26372-26384, 2013.

Figure legends

Figure 1. *Ae1*$^{+/R607H}$ and *Ae1*$^{R607H/R607H}$ knock-in mice show incomplete distal tubular acidosis.

(**A**) Position of the human R589H mutation within the putative topology of AE1 according to the model presented by [32]. (**B**) Alignment of human AE1 R589 with murine Ae1 R607. (**C**) Introduction of the modified codon verified by Sanger sequencing. (**D**) Red blood cells of heterozygous and homozygous knock-in mice displayed normal morphology. Scale bar: 10 µm. (**E-H**) After 3 days under standard conditions to determine baseline values, *Ae1*$^{+/+}$ (n=6; black diamond), *Ae1*$^{+/R607H}$ (n=10; blue square) and *Ae1*$^{R607H/R607H}$ (n=8; red triangle) mice were acid-challenged for 6 days with 0.28 M NH_4Cl in drinking water. (E) Blood pH. (F) Blood [Cl^-] in mM. (G) Urine pH. (H) Urinary NH_4^+ excretion. Data are presented as mean ± SEM. **P<0.01, ***P<0.001, ****P<0.0001 vs *Ae1*$^{+/+}$ and $^{\#}$P<0.05, $^{\#\#}$P<0.01 vs *Ae1*$^{+/R607H}$ (Two-way ANOVA).

Figure 2. The bicarbonate transporter NBCn1 shows a compensatory increase in *Ae1*$^{+/R607H}$ and *Ae1*$^{R607H/R607H}$ mice.

(**A**) Protein abundance of pH relevant transporters NBC, NHE3, NBCn1 and AE2 in protein lysates from whole kidney tissue under baseline conditions. *Ae1*$^{+/+}$ (n=5), *Ae1*$^{+/R607H}$ (n=5), and *Ae1*$^{R607H/R607H}$ (n=4). (**B**) Quantification of NBC, NHE3, NBCn1, and AE2 protein abundance. The abundance of NBCn1 is strongly increased in *Ae1*$^{+/R607H}$ and *Ae1*$^{R607H/R607H}$ mice. Data are presented as mean ± SEM. ***P<0.001, ****P<0.0001 vs *Ae1*$^{+/+}$ (One-way ANOVA). (**C**) Fluorescence intensity for NBCn1 is increased in the TAL. Ae1 (green), NBCn1 (red). Scale bar: 30 µm.

Figure 3. The R607H/R589H variant is correctly targeted to the basolateral plasma membrane.

(**A**-**F**) High magnification images of cortical collecting duct (A-C) and inner stripe of the outer medulla (D-F) in *Ae1*$^{+/+}$, *Ae1*$^{+/R607H}$ and *Ae1*$^{R607H/R607H}$ showing that Ae1 R607H is localized to the basolateral pole of A-ICs. Scale bar: 10 µm. (**G**-**I**) The basolateral targeting of Ae1 R607H is evident from

immunogold labeling in cortical A-ICs. Scale bar: 250 nm. (**J**-**M**) M1 (J,K) or mIMCD-3 (L,M) cells expressing either human kAE1 WT-myc or R589H-HA were grown to confluency for 7 days on semi-permeable filters prior to fixation, permeabilization and detection of kAE1 with either mouse anti-myc or anti-HA antibody, followed by Cy3-coupled anti-Ig (red). Nuclei were stained with DAPI. Scale bar: 10 µm.

Figure 4. The R607H/R589H mutation impairs AE1-dependent chloride bicarbonate exchange activity in vivo.

(**A**) Representative (BCECF fluorescence ratio) intracellular pH traces from Cl^- /HCO_3^- exchange experiments performed on mIMCD-3, mIMCD-3 kAE1 WT, mIMCD-3 kAE1 R589H or mIMCD-3 co-expressing kAE1 WT and R589H. The white and black rectangles above indicate incubations with NaCl and sodium gluconate containing solutions, respectively. (**B**) Transport rates of kAE1 WT, R589H or WT and R589H mutant are all similar in mIMCD-3 cells. (**C**) Anion-exchange traces of resealed red blood cell ghosts. (**D**) Anion-exchange activity is identical in ghosts prepared from either *Ae1*$^{+/+}$, *Ae1*$^{+/R607H}$ and *Ae1*$^{R607H/R607H}$ mice. (**E**) Fluorescence intensity of FACS-sorted red blood cells labelled with anti-Diego antibodies directed against different extracellular AE1 epitopes. (**F**) Quantitative comparison of AE1 surface expression in red blood cells from WT, *Ae1*$^{+/R607H}$ and *Ae1*$^{R607H/R607H}$ mice did not reveal differences among genotypes (n.s., one-way ANOVA and Tukey's multiple comparisons test). Data are shown as mean ± SEM from a minimum of 3 independent experiments (*P<0.05, **P<0.01 versus control, one-way ANOVA).

Figure 5. AE1 expression is reduced in the kidney of Ae1$^{+/R607H}$ and Ae1$^{R607H/R607H}$ mice.

(**A,B**) Quantitative RT-PCR shows that relative cortical *Ae1* transcript abundance in *Ae1*$^{+/R607H}$ mice is only 40 % of wild-type levels and 15 % in *Ae1*$^{R607H/R607}$ mice (A). Relative *Ae1* medullary transcript abundance in *Ae1*$^{+/R607H}$ is 70 % of wild-type levels and 35 % in *Ae1*$^{R607H/R607}$ (B). Data are presented as means ± SEM; n=3 each. (**C-D**) Ae1 protein abundance analyzed in protein lysates from cortex and medulla, is drastically reduced in

the cortex and only slightly less so in the medulla of *Ae1*$^{+/R607H}$ and *Ae1*$^{R607H/R607}$ mice compared to wild-type. Data are presented as means ± SEM; n=5 per genotype. (**E-F**) Consistent with immunoblot results, Ae1 immunoreactivity (red) in cortex (upper panels) and medulla (lower panels) is decreased in *Ae1*$^{+/R607H}$ and *Ae1*$^{R607H/R607H}$ mice relative to that in *Ae1*$^{+/+}$ mice. Scale bar: 75 µm. (**F,G**) Quantification of time-dependent relative AE1 abundance in M1 (F) and mIMCD3 (G) cells incubated with protein synthesis inhibitor, cycloheximide. Data are presented as means ± SEM; n=3 each. *P<0.05, **P<0.01, ***P<0.005, ****P<0.001 (One-way ANOVA and Tukey's multiple comparison).

Figure 6. Apical sorting of the proton pump is compromised in *Ae1*$^{+/R607H}$ and *Ae1*$^{R607H/R607H}$ mice

(A-C) The B1 subunit of the V-ATPase of acid challenged WT mice almost exclusively localized to the apical domain of A-ICs in the cortex. In *Ae1*$^{+/R607H}$ and *Ae1*$^{R607H/R607H}$ mice, however, this shift to the apical domain did not occur, suggesting a secondary targeting defect of the proton pump in *Ae1*$^{+/R607H}$ and *Ae1*$^{R607H/R607H}$ mice. Scale bar: 10 µm. (**D**-**I**) Immunogold labeling of the A subunit of the V-type-ATPase**.** (D-F) Overview of A-ICs from WT, *Ae1*$^{+/R607H}$ and *Ae1*$^{R607H/R607H}$ mice. (G-I) Higher magnification view of the apical cell pole. Scale bar: 2 µm. (J-L) Higher magnification view of the basolateral cell pole. Scale bar: 1 µm. (**J**) Renal cortex immunoblot shows reduced B1 subunit expression in both heterozygous and homozygous mice *P<0.05, ****P<0.0001 compared to the WT (One-way ANOVA and Tukey's multiple comparison).

Figure 7. Cortical collecting ducts of *Ae1*$^{+/R607H}$ and *Ae1*$^{R607H/R607H}$ mice are depleted of A-ICs

(**A**) Co-staining for Ae1 (red), Pendrin (blue), and the E-subunit (green) of the V-type ATPase. Pendrin-negative cells that stain for the E-subunit also label for Ae1 and thus represent A-ICs. Scale bar: 25 µm. (**B**) Co-staining for Ae1 (red), Pendrin (blue), and Aquaporin 2 (green). Scale bar: 25 µm. (**C**,**D**) Quantification of A-ICs, B-ICs, and principal cells in the cortex at baseline (C) and after acid challenge (D). The number of cortical A-ICs is strongly reduced

in *Ae1*$^{+/R607H}$ and *Ae1*$^{R607H/R607H}$ mice. (**E**) Cross-sectional area of individual A-ICs was increased in mutant compared to wild-type mice in the inner stripe of the outer medulla (ISOM). n=30 cells each. *P<0.05, **P<0.01, ***P<0.001 (One-way ANOVA and Tukey's multiple comparison).

Figure 8. A-ICs accumulate p62^{+} structures in *Ae1*$^{+/R607H}$ and *Ae1*$^{R607H/R607H}$ mice

(**A-I**) Compared to WT (**A,D,G**) the ultrastructural architecture of A-ICs of *Ae1*$^{+/R607H}$ (**B,E,H**) and *Ae1*$^{R607H/R607H}$ (**C,F,I**) mice is characterized by a depletion of the regular intracellular vesicles (arrow) and accumulation of lysosomal inclusions (arrowheads) and multilamellar bodies (asterisks). Scale bars: 2 µm (A-C) and 1 µm (D-F) and 500 nm (G-I). (**J**-**L**) Accumulation of p62^{+} deposits in Ae1-positive cells in the renal cortex of *Ae1*$^{+/R607H}$ and *Ae1*$^{R607H/R607H}$ mice but not in Ae1$^{+/+}$ mice. Scale bar: 25 µm. (**M-O**) p62 positive structures in the renal cortex of *Ae1*$^{+/R607H}$ and *Ae1*$^{R607H/R607H}$ mice partially co-localize with Ubiquitin. Scale bar: 10 µm.

Table 1. Baseline characterization of *Ae1*$^{+/R607H}$ and *Ae1*$^{R607H/R607H}$ mice

In the basal state *Ae1*$^{+/R607H}$ and *Ae1*$^{R607H/R607H}$ mice have no detectable alterations in acid-base parameters revealing that, as in humans, R607H mutation causes incomplete dRTA with a higher urinary pH. The increase in blood chloride levels is consistent with the presence of a mild hyperchloremic metabolic acidosis. Values are means ± SEM, numbers of mice are indicated in brackets. *P<0.05, ****P<0.0001, vs Ae1$^{+/+}$ (age 3-5 months, One-way ANOVA).

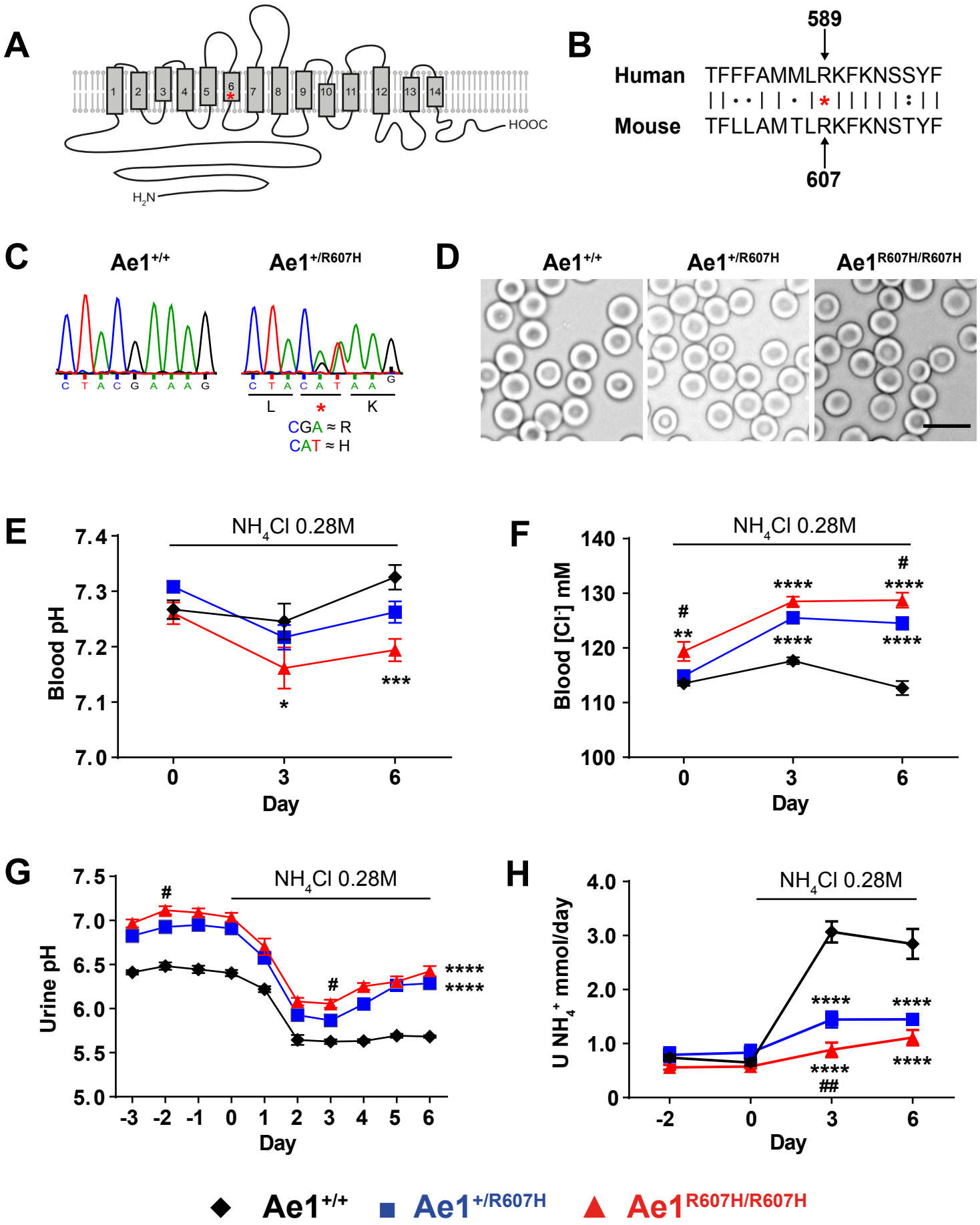
A
1 2 3 4 5 6 7 8 9 10 11 12 13 14
*
HOOC
H2N
B
589
Human TFFFAMMLRKFKNSSYF
Mouse TFLLAMTLRKFKNSTYF
607
C
Ae1+/+
Ae1+/R607H
C T A C G A A A G
C T A C A T A A G
L * K
CGA ≈ R
CAT ≈ H
D
Ae1+/+
Ae1+/R607H
Ae1R607H/R607H
E
NH4Cl 0.28M
Blood pH
7.4
7.3
7.2
7.1
7.0
0 3 6
Day
*
***
F
NH4Cl 0.28M
Blood [Cl-] mM
140
130
120
110
100
0 3 6
Day
#
**
****
****
#
****
****
G
NH4Cl 0.28M
Urine pH
7.5
7.0
6.5
6.0
5.5
5.0
-3 -2 -1 0 1 2 3 4 5 6
Day
#
#
****
****
H
NH4Cl 0.28M
U NH4+ mmol/day
4.0
3.0
2.0
1.0
0
-2 0 3 6
Day
****
****
****
****
##
Ae1+/+
Ae1+/R607H
Ae1R607H/R607H

Figure: 1

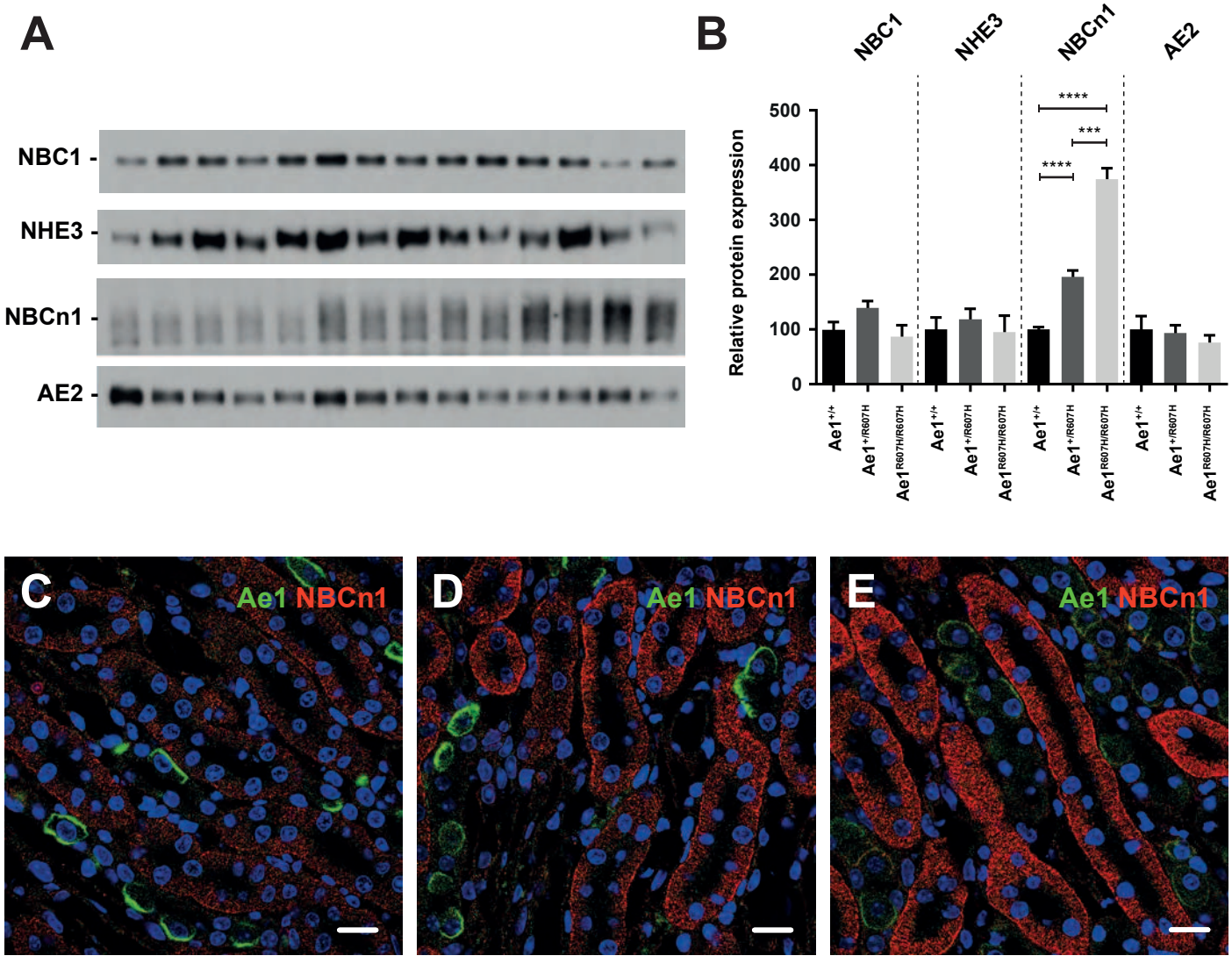
A
NBC1
NHE3
NBCn1
AE2
B
NBC1
NHE3
NBCn1
AE2
Relative protein expression
500
400
300
200
100
0
****
***
****
Ae1+/+
Ae1+/R607H
Ae1R607H/R607H
C
Ae1 NBCn1
D
Ae1 NBCn1
E
Ae1 NBCn1

Figure: 2

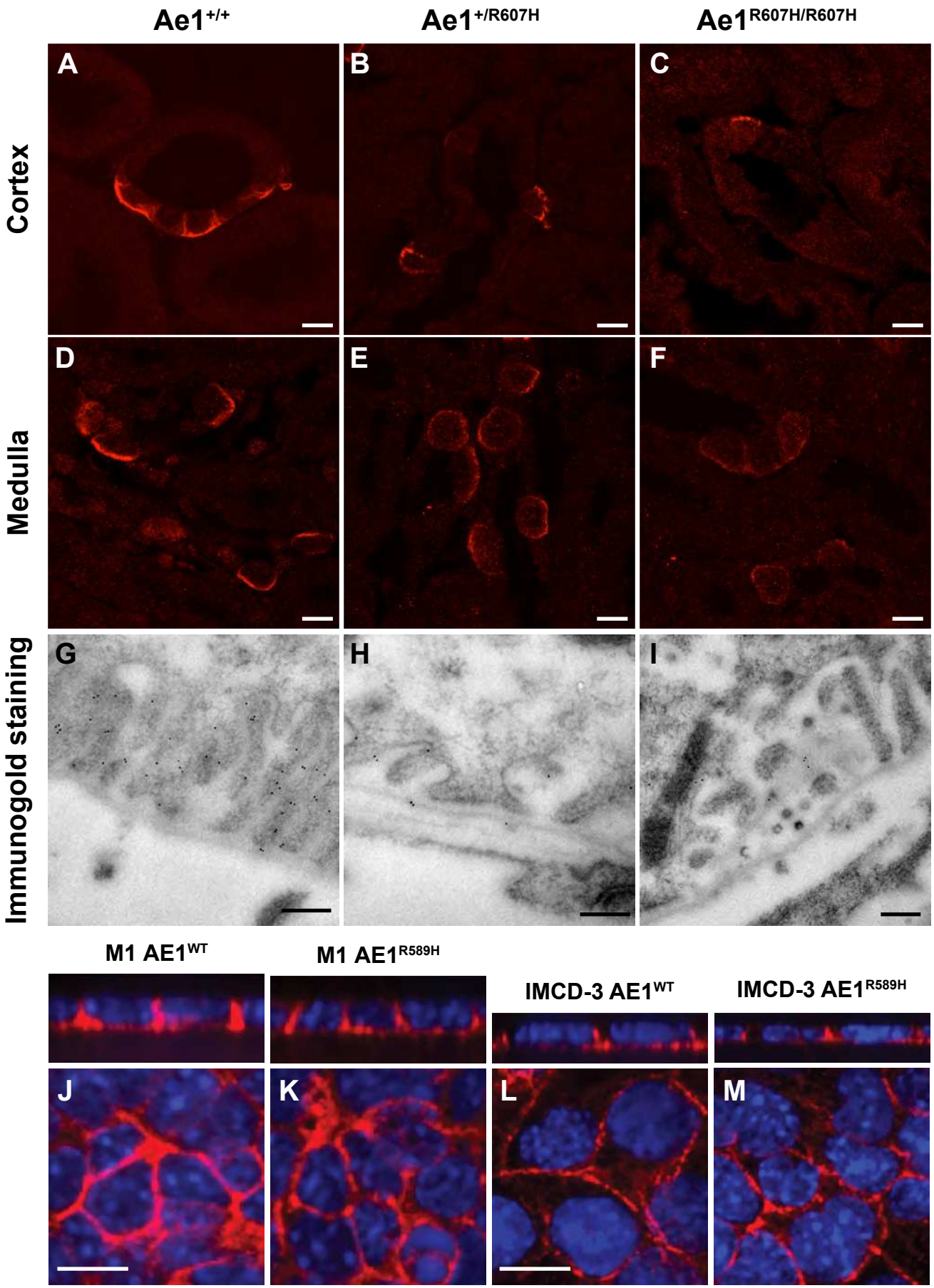
Ae1+/+
Ae1+/R607H
Ae1R607H/R607H
Cortex
Medulla
Immunogold staining
A
B
C
D
E
F
G
H
I
M1 AE1WT
M1 AE1R589H
IMCD-3 AE1WT
IMCD-3 AE1R589H
J
K
L
M

Figure: 3

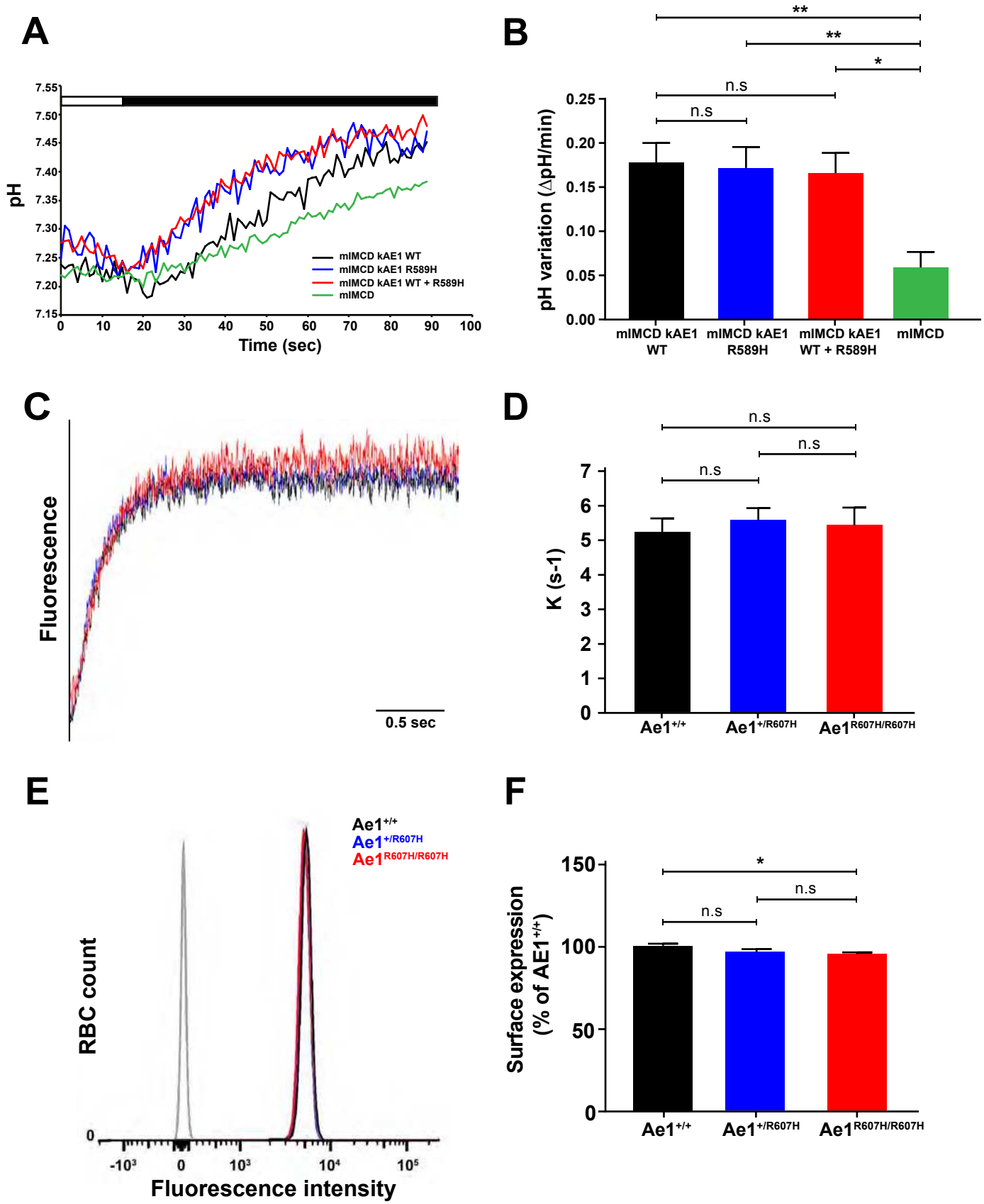
A
pH
Time (sec)
mIMCD kAE1 WT
mIMCD kAE1 R589H
mIMCD kAE1 WT + R589H
mIMCD
B
pH variation (ΔpH/min)
n.s
**
*
mIMCD kAE1 WT
mIMCD kAE1 R589H
mIMCD kAE1 WT + R589H
mIMCD
C
Fluorescence
0.5 sec
D
K (s-1)
n.s
Ae1+/+
Ae1+/R607H
Ae1R607H/R607H
E
RBC count
Fluorescence intensity
Ae1+/+
Ae1+/R607H
Ae1R607H/R607H
F
Surface expression (% of AE1+/+)
n.s
*
Ae1+/+
Ae1+/R607H
Ae1R607H/R607H

Figure: 4

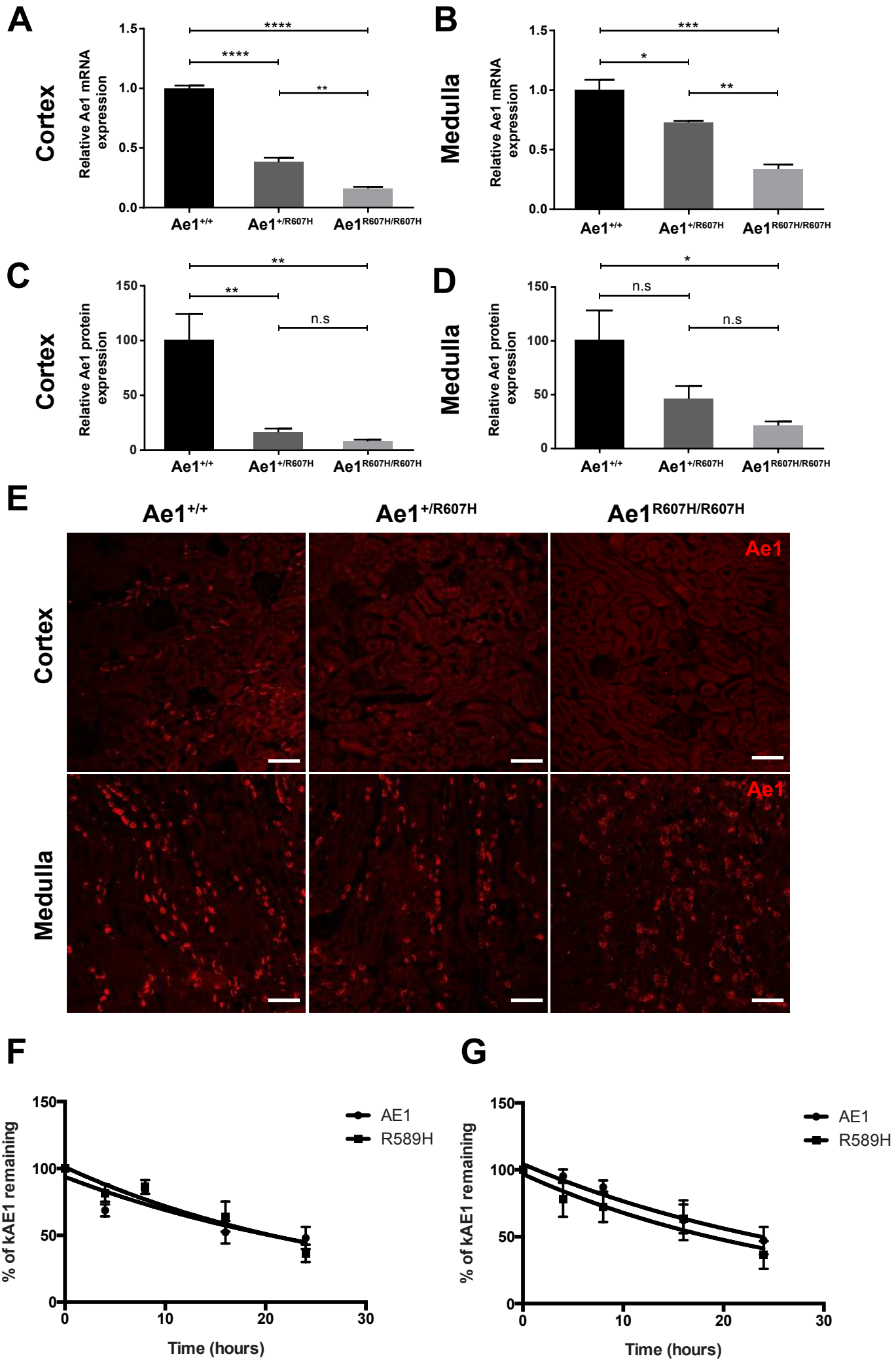
A
Cortex
Relative Ae1 mRNA expression
1.5
1.0
0.5
0.0
****
****
**
Ae1+/+
Ae1+/R607H
Ae1R607H/R607H
B
Medulla
Relative Ae1 mRNA expression
***
*
**
C
Cortex
Relative Ae1 protein expression
150
100
50
0
**
**
n.s
D
Medulla
Relative Ae1 protein expression
*
n.s
n.s
E
Ae1+/+
Ae1+/R607H
Ae1R607H/R607H
Cortex
Medulla
Ae1
F
% of kAE1 remaining
Time (hours)
AE1
R589H
G
% of kAE1 remaining
Time (hours)
AE1
R589H

Figure: 5

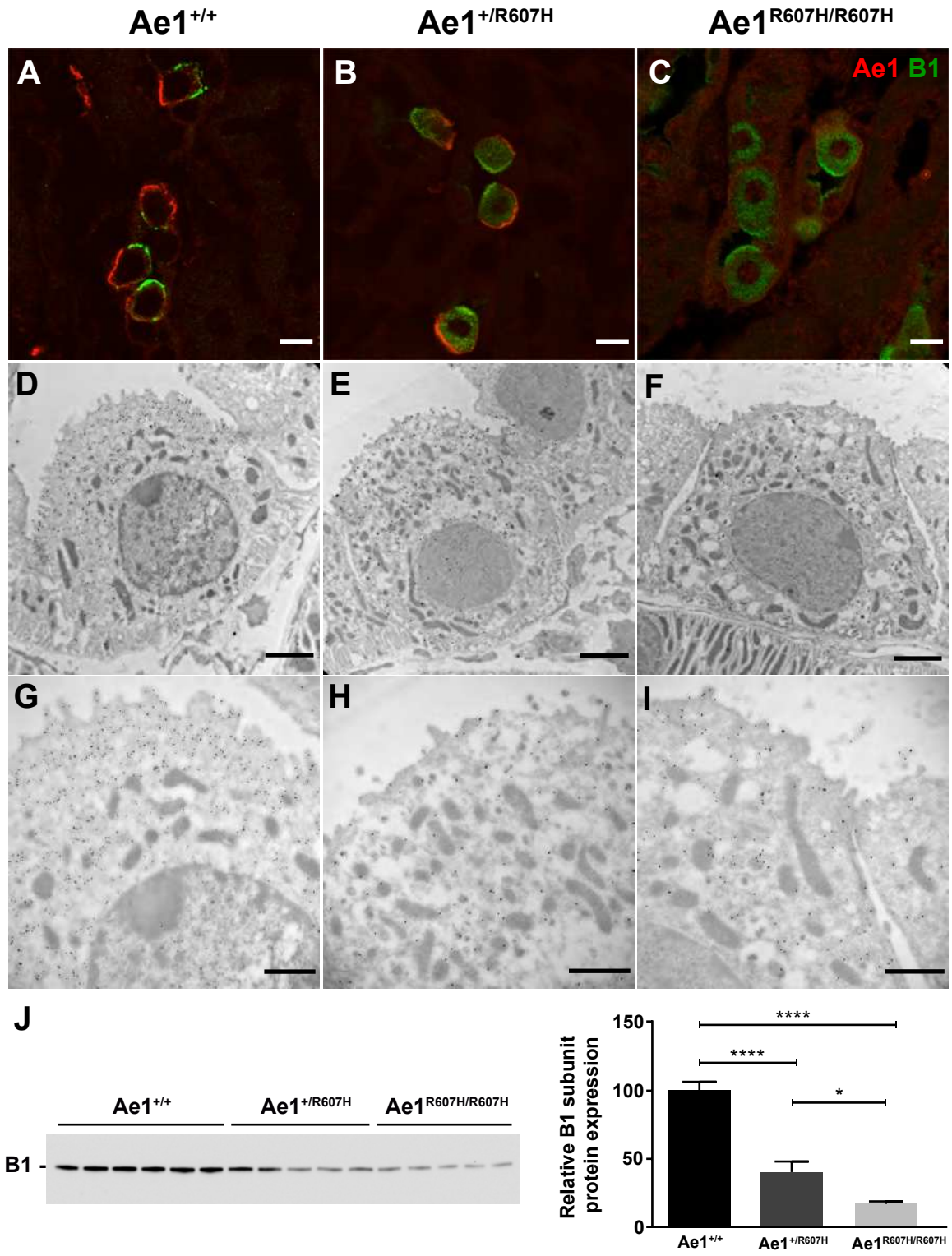
Ae1+/+
Ae1+/R607H
Ae1R607H/R607H
A
B
C
Ae1 B1
D
E
F
G
H
I
J
Ae1+/+
Ae1+/R607H
Ae1R607H/R607H
B1
Relative B1 subunit protein expression
150
100
50
0
****
****
*
Ae1+/+
Ae1+/R607H
Ae1R607H/R607H

Figure: 6

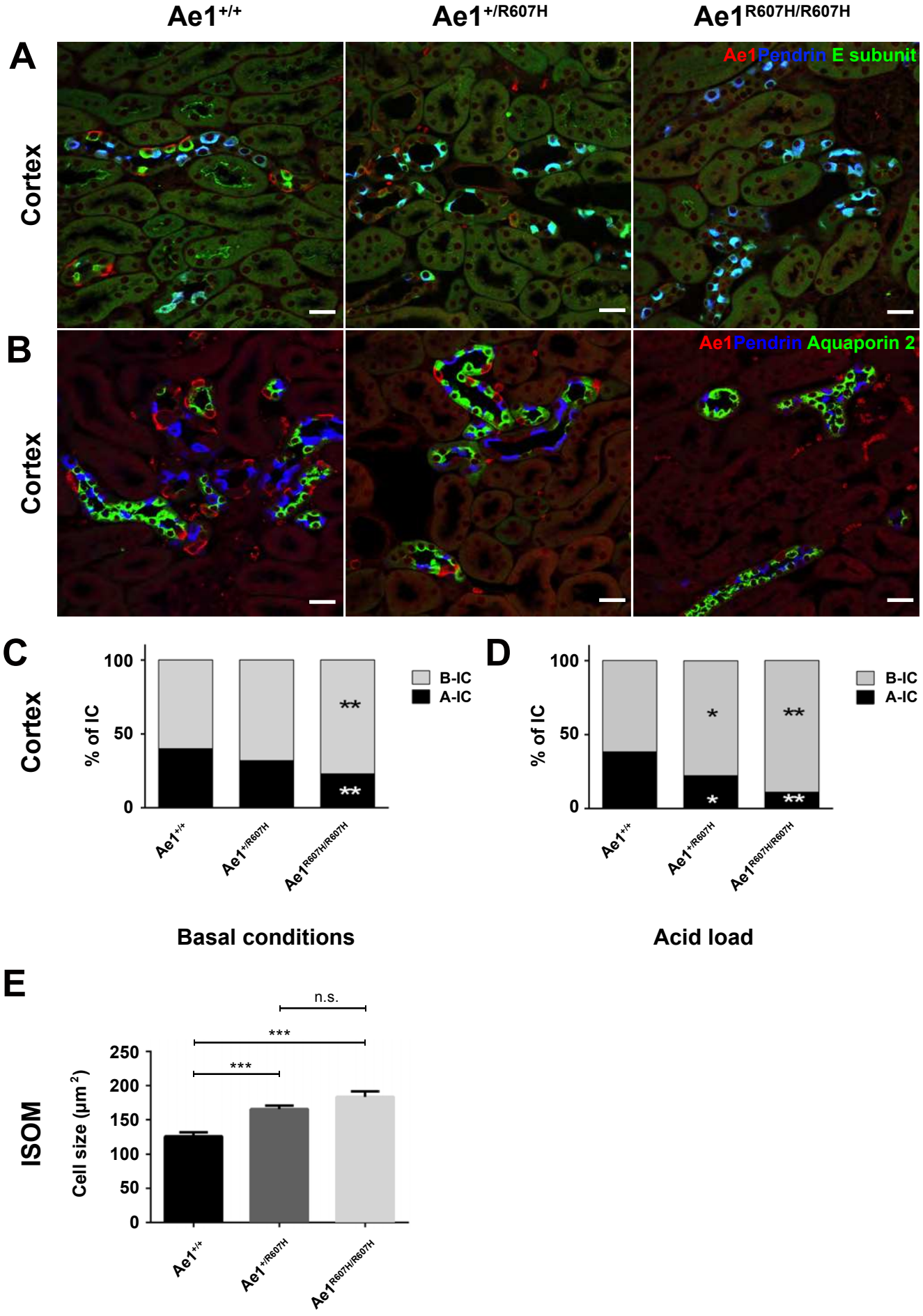
Ae1+/+
Ae1+/R607H
Ae1R607H/R607H
A
Cortex
Ae1Pendrin E subunit
B
Cortex
Ae1Pendrin Aquaporin 2
C
Cortex
% of IC
100
50
0
B-IC
A-IC
**
**
Ae1+/+
Ae1+/R607H
Ae1R607H/R607H
Basal conditions
D
% of IC
100
50
0
B-IC
A-IC
*
**
*
**
Ae1+/+
Ae1+/R607H
Ae1R607H/R607H
Acid load
E
ISOM
Cell size (µm2)
250
200
150
100
50
0
n.s.
***
***
Ae1+/+
Ae1+/R607H
Ae1R607H/R607H

Figure: 7

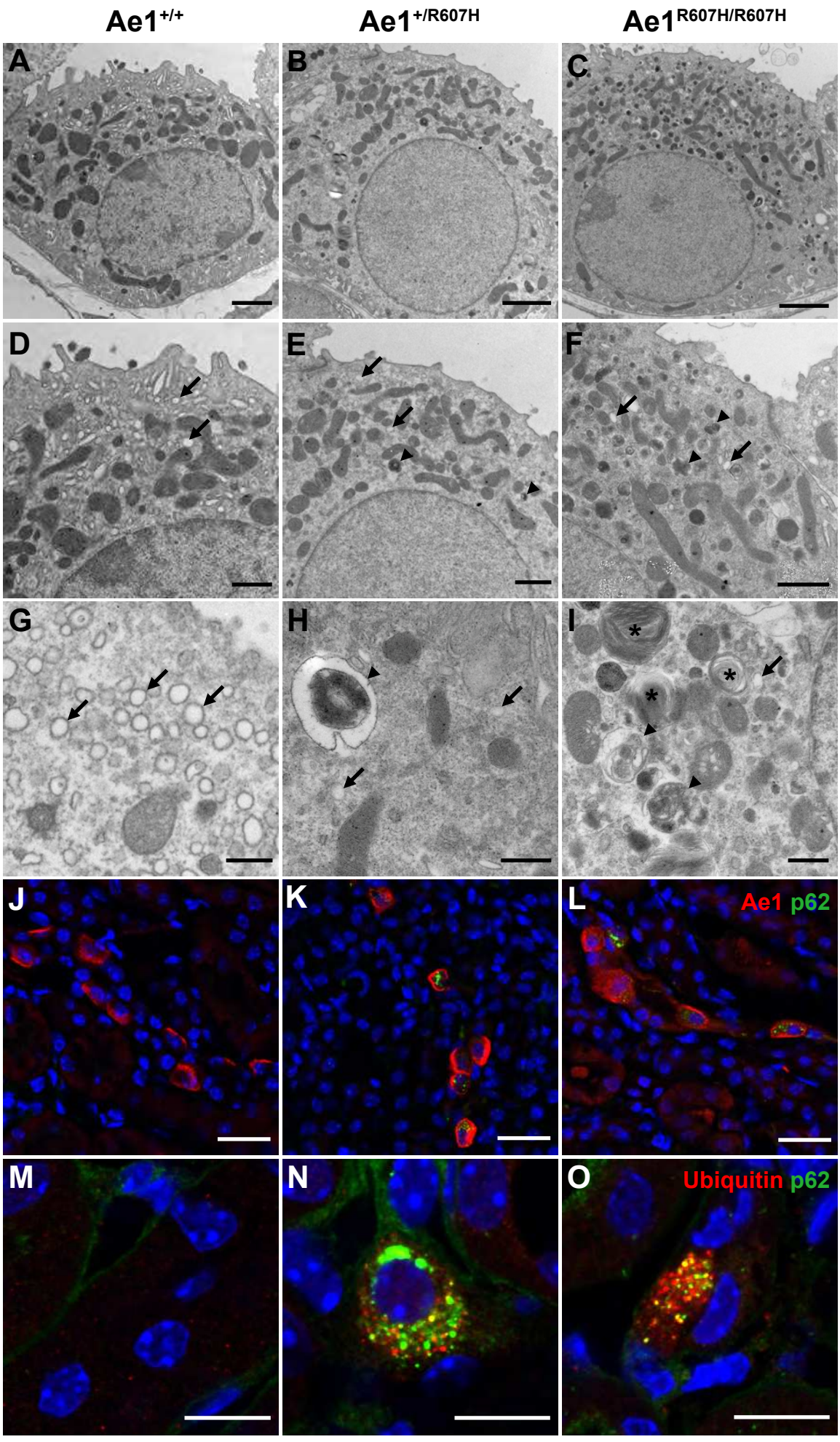
Ae1+/+
Ae1+/R607H
Ae1R607H/R607H
A
B
C
D
E
F
G
H
I
J
K
L
Ae1 p62
M
N
O
Ubiquitin p62

Figure: 8

			$Ae1^{+/+}$		$Ae1^{+/R607H}$		$Ae1^{R607H/R607H}$	
General	**BW**	g	24.45 ± 0.39	(6)	24.11 ± 0.31	(10)	23.76 ± 0.48	(8)
	Food Intake	g/gBW/d	0.17 ± 0.01	(6)	0.17 ± 0.01	(10)	0.17 ± 0.01	(8)
	Water Intake	ml/gBW/d	0.18 ± 0.02	(6)	0.18 ± 0.01	(10)	0.18 ± 0.01	(8)
Blood	**Hct**	%	45 ± 0.65	(13)	45 ± 0.28	(12)	47 ± 0.80	(9)
	Hb	g/dl	15.1 ± 0.16	(9)	15.08 ± 0.16	(13)	15.3 ± 0.36	(15)
	Na^+	mM	146 ± 0.36	(13)	147 ± 0.46	(12)	147 ± 0.47	(9)
	Cl^-	mM	111 ± 0.74	(13)	115 ± 0.77*	(13)	118 ± 1.44****	(13)
	K^+	mM	4.56 ± 0.10	(7)	4.75 ± 0.07	(7)	4.45 ± 0.08	(5)
	Ca^{2+}	mM	1.25 ± 0.01	(13)	1.26 ± 0.01	(13)	1.25 ± 0.01	(12)
	pH		7.32 ± 0.02	(13)	7.32 ± 0.01	(13)	7.29 ± 0.02	(12)
	pCO_2	mmHg	43 ± 1.19	(12)	46 ± 1.16	(12)	43 ± 0.92	(11)
	HCO_3^-	mM	22 ± 0.55	(13)	22 ± 0.44	(12)	21 ± 0.70	(12)
Urine	**Urine Output**	ml/gBW/d	0.075 ± 0.008	(6)	0.069 ± 0.005	(10)	0.065 ± 0.004	(8)
	Urine Osm	mOsm/kgH_2O	3178 ± 383	(6)	2891 ± 246	(10)	2670 ± 108	(8)
	Urine pH		6.45 ± 0.04	(6)	6.95 ± 0.05****	(10)	7.09 ± 0.05****	(8)
	Na^+/Creat	mmol/mmol	17 ± 1.19	(6)	20 ± 0.68	(10)	21 ± 0.93	(8)
	K^+/Creat	mmol/mmol	57 ± 11.69	(6)	63 ± 6.41	(10)	64 ± 5.99	(8)
	Ca^{2+}/Creat	mmol/mmol	0.17 ± 0.02	(6)	0.15 ± 0.01	(10)	0.10 ± 0.01*	(8)

Supplementary Information

Materials and Methods

All animal experiments were approved by the Thüringer Landesamt für Lebensmittelsicherheit und Verbraucherschutz (TLLV) in Germany.

Generation of Ae1^{R607H} knock-in mice

A clone isolated from a 129/SvJ mouse genomic λ library (Stratagene, now Agilent, Santa Clara, CA, USA) was used to construct the targeting vector. A ~13.25 kb fragment including exons 2-18 of the *Ae1* gene was cloned into the pKO-V901 plasmid (Lexicon Genetics, The Woodlands, TX, USA) with a phosphoglycerate kinase (pgk) promoter-driven diphtheria toxin A cassette. A pgk promoter-driven neomycin resistance cassette flanked by loxP sites was inserted into the *Pci*I site of intron 9. The R607H point mutation was introduced by site-directed mutagenesis into a subcloned *Bst*Z17I-*Spe*I fragment (1541 bp) harboring exon 14. The construct was linearized with *Not*I and electroporated into R1 mouse embryonic stem (ES) cells. Neomycin-resistant clones were analyzed by Southern blot using *Hind*III and an external probe of 779 bp (Chromosome 11, 102350002-102350780) was amplified with primers "Ae1_SB1_for" (5'-GTC TAT ATG CAG GCC TTT GTC-3') and "Ae1_SB1_rev" (5'-CAT GAA AAG TGT CCT CCG T-3'). Two correctly targeted ES cell clones were injected into C57BL/6 blastocysts to generate chimeras. Chimeric mice were mated to a cre-Deleter mouse strain to remove the selection cassette (1). Studies were performed in a mixed 129Sv/C57BL/6 background in the F4 and F5 generation. Genotypes were determined by PCR of tail biopsy DNA. For PCR genotyping, the forward primer F1 (5′-TAG CTC CTT CTA CCC CAC CCA-3′) and the reverse primer R1 (5′-CCA GAG GTA CAT GGT AAA ACA TTG TC-3′) were used in a single PCR mix allowing detection of the 189 bp wild-type allele and the 320 bp knock-in (KI) allele. Detection of the introduced point mutation was performed by Sanger sequencing of the 498 bp PCR product amplified by forward primer F1 (5′-GCT CAA GTC AAG GCT TGG ATG G-3′) and reverse primer R1 (5′- CAA GGA TTC TGC TCA TCC GGA-3′).

NH_4Cl loading

We initially planned to study 8 mice of each genotype. However, as insufficient numbers of wild-type mice were available at the time metabolic cage experiments began, we increased the number of heterozygous mice. Thus, n=6 *Slc4a1*$^{+/+}$; n=10 *Slc4a1*$^{R607H/+}$; n=8 *Slc4a1*$^{R607H/R607H}$ 3-month-old male littermates were housed in metabolic cages (Tecniplast, Buguggiate, Italy). Urine was collected daily under mineral oil. After adjustment to metabolic cages and recording of baseline parameters drinking water was supplemented with 0.28 M NH_4Cl for 6 days.

The pH of urine samples was measured with a pH microelectrode (InLab Micro pH, Mettler Toledo, Viroflay, France) and samples were immediately frozen before further analysis. Retro-orbital blood was collected at days 3 and 6 following acid loading and analyzed with the ABL 77 pH/blood-gas analyser (Radiometer, Copenhagen, Denmark). Urinary ammonium and titratable acid was measured by titration with a DL 55 titrator (Mettler Toledo, Viroflay, France). Urine osmolalities were determined by freezing point osmometer (Roebling, Berlin, Germany). Urine creatinine was measured by Jaffé colorimetric method. Urinary Na^+ and K^+ were measured by flame photometry (IL 943; Global Medical Instrumentation, Ramsey, MN, USA). Urine aldosterone was measured via RIA (DPC Dade Behring, now Siemens Healthcare, Erlangen, Germany).

Histology and immunohistochemistry

Kidneys were fixed by retrograde perfusion of the aorta with 4 % PFA in phosphate buffer. Dissected kidneys were washed in ice-cold PBS for 30 minutes and flash frozen in isopentane cooled with liquid nitrogen. 6 µm thick cryosections were subjected to Masson-Goldner stain or von Kossa stain. Kidney sections from a4 knockout mice served as a positive control (2). For immunohistochemistry, cryosections were blocked with goat or donkey serum (3). Sections were incubated overnight at 4°C with primary antibody, washed with PBS, incubated with fluorophore-conjugated secondary antibody, washed with PBS and then mounted with Glycergel mounting medium (DAKO/Agilent, Santa Clara, CA, USA). Each experiment included three mice per group. Representative images were acquired with a Confocal SP8 workstation (Leica, Wetzlar, Germany).

Cell culture

M1 (cortical collecting duct cells, ATCC CRL-2038) and mIMCD-3 cells (ATCC CRL-2123) underwent infection with mouse moloney leukemia virus to induce quasi-stable expression of human kidney anion exchanger 1 (kAE1) WT-myc, of R589H-HA (the human equivalent of R607H), or of both kAE1 WT-myc and kAE1 R589H-HA, as previously described (4). However, despite continued G418 exposure of cell cultures (1 mg/ml for M1 cells; 2 mg/ml for mIMCD-3 cells), kAE1 protein expression declined over a two-to-three week period. For immunostaining, cells were grown for 7 days on semi-permeable filter supports, fixed with 4 % paraformaldehyde, quenched, rinsed, and blocked with 0.1 % Triton X-100, followed by 1 % bovine serum albumin in PBS. Epitope-tagged kAE1 proteins were detected either with mouse anti-myc (Cell Signalling, Danvers, MA, USA) or mouse anti-HA antibodies (Covance, Princeton, NJ, USA), each followed by Cy3-coupled anti-mouse Ig (Jackson ImmunoResearch laboratories, West Grove, PA, USA). Samples were examined with an IX81 microscope (Olympus, Tokyo, Japan) equipped with a Nipkow spinning-disk (Quorum Technologies, Guelph, Canada).

Counting of intercalated and principal cells

Kidney sections were co-stained either for AE1, pendrin, and V-type ATPase E subunit (Atp6v1e1) or for AE1, pendrin, and AQP2. Ten random fields from cortex and inner stripe of the outer medulla (ISOM) were acquired at 20X magnification. Numbers of principal cells (defined by apical expression of AQP2), type A intercalated cells (basolateral AE1 expression), and type B intercalated cells (apical pendrin expression) were counted (n=3 mice per genotype).

Electron microscopy

After perfusion *in situ* with 4 % PFA as above, tissues were shipped in fixative to Boston, where they were further fixed in 2 % glutaraldehyde in 0.1 M sodium cacodylate pH 7.4 (Electron Microscopy Sciences, Hatfield, PA, USA). Tissues were then rinsed in cacodylate buffer and post-fixed in 1 % osmium tetroxide (Electron Microscopy Sciences) in 0.1 M cacodylate buffer for 1 h at room temperature, and then rinsed as above. After washing in double distilled water, the samples were stained, en bloc, in an aqueous solution of 2 % uranyl acetate for 1 h at room

temperature. The samples were rinsed in water and dehydrated through a graded ethanol series to 100 % ethanol, then infiltrated with EPON (Ted Pella Inc., Redding, CA USA) in a solution of 1:1, EPON: 100 % ethanol overnight. They were then placed in fresh EPON for several hours and subsequently embedded in EPON overnight in a 60°C oven. Ultrathin sections were cut on a Leica EMUC7 ultramicrotome (Leica), collected on formvar-coated grids, stained with lead citrate and uranyl acetate, and examined at 80 kV in a JEOL 1011 transmission electron microscope (TEM; JEOL, Peabody, MA, USA). Images were acquired using an AMT digital imaging system (Advanced Microscopy Techniques, Danvers, MA, USA).
For immunogold staining, samples fixed in 4 % paraformaldehyde alone were embedded in LRWhite resin as previously described (5). Ultrathin sections were incubated 2 h with anti-AE1 or V-type ATPase antibodies (6), rinsed, and incubated 45 min with gold-labeled goat anti-guinea-pig Ig (Ted Pella). Sections were rinsed again in PBS and counterstained with lead citrate and uranyl acetate before imaging as above in the JEOL 1001 TEM.

Immunoblotting

Mice were perfused transcardially with PBS at RT. Perfused kidneys were placed in ice-cold PBS and homogenized in ice-cold isolation buffer (250 mM sucrose, 20 mM Tris-Hepes, pH 7.4) supplemented with protease inhibitor cocktail (Complete; Roche Diagnostics, Risch-Rotkreuz, Switzerland) and phosphatase inhibitor cocktail (PhosSTOP; Roche Diagnostics). Cellular debris was removed by centrifugation at 4,000 g for 15 min at 4°C. Membrane-enriched fractions were prepared by centrifugation at 17,000 g for 30 min at 4°C. Protein concentration was determined using the Bradford protein assay (microBradford, BioRad, Hercules, CA, USA). Total homogenates and membrane-enriched fractions were prepared with 6x SDS-loading buffer (0.375 mM Tris-HCl pH 6.8, 12 % SDS, 0.6 M dithiothreitol, 60 % glycerol and bromophenol blue) and incubated 30 min at room temperature. 15-30 µg of protein were loaded on 10 % polyacrylamide gels (XCell *SureLock* Mini-cell; Invitrogen Life Technologies, Carlsbad, CA, USA) separated and blotted onto a nitrocellulose membrane. Membranes were blocked with 5 % milk in TBS and incubated overnight at 4°C with the primary antibody. The secondary horseradish-conjugated anti-Ig antibody was incubated on membranes for 2 hrs at RT, detected with Pierce ECL

Western Blotting Substrate (Thermo Scientific, Waltham, MA, USA), and analyzed by LAS 4000 ImageQuant (GE Healthcare, Little Chalfont, UK).

Half-life measurement

M1 or mIMCD-3 cells expressing kAE1 WT-myc or kAE1 R589H-HA were plated to sub-confluency on 6-well plates, then incubated 0, 4, 8, 16 or 24h with 10 µg/ml cycloheximide in DMEM:F12 culture medium supplemented with 10 % fetal bovine serum and 1 mg/ml penicillin/streptomycin. Cells were lysed in PBS containing 1 % Triton X-100, 1 µg/ml aprotinin, 2 µg/ml leupeptin, 1 µg/ml pepstatin A, and 100 µg/ml PMSF. kAE1 polypeptides were subjected to immunoblot analysis using mouse anti-HA or anti-myc antibody, followed by horseradish peroxidase-coupled anti-mouse Ig (Cell Signaling). Bound peroxidase was detected by enhanced chemiluminescence (ECL Prime; GE Healthcare) and relative band intensities were analyzed with ImageJ.

AE1-mediated transport activity in red blood cells by stopped-flow analysis

200 µl mouse blood was washed three times in PBS. Washed red blood cells were resuspended in 32 ml hypotonic lysis buffer (7 mM KCl, 10 mM Hepes/KOH, pH 7.2) for 40 min on ice, followed by resealing for 1h at 37°C in resealing buffer (100 mM KCl, 10 mM Hepes/KOH, pH 7.2, 1 mM $MgCl_2$ and 2 mg/ml bovine carbonic anhydrase) containing 0.15 mM of the fluorescent pH sensitive dye pyranine (1-hydroxypyrene-3,6,8-trisulfonic acid, Sigma-Aldrich, St. Louis, MO, USA). After three washes in ice-cold incubation buffer (100 mM KCl, 10 mM Hepes/KOH, pH 7.2), resealed ghosts were kept on ice until stopped-flow experiments were performed (7) at 30°C (SFM400; Bio-logic, Grenoble, France). Excitation was at 465 nm and emitted light was filtered with a 520 nm cut-off filter. For measurement of HCO_3^-/Cl^- exchange activity, dye-loaded ghosts resuspended in 3 ml “chloride buffer” (100 mM KCl and 10 mM HEPES/KOH pH 7.2) were rapidly mixed with an equal volume of bicarbonate buffer (100 mM $KHCO_3$ and 10 mM HEPES/HCl pH 7.2), generating an inwardly directed HCO_3^-/CO_2 gradient of 50 mEq/L and an outwardly directed Cl^- gradient of equal magnitude. Data from six-to-eight time courses were averaged and fit to a mono-exponential function using the simplex procedure of Biokine software (Bio-logic).

Surface AE1 expression on erythrocytes was determined by immunostaining with an anti-Diego b (Dib) antibody followed by flow cytometric analysis on a FACSCanto II flow cytometer (Becton-Dickinson, Franklin Lakes, NJ, USA). Secondary antibodies were goat anti-human PE-conjugated F(ab')2 fragments (Beckman Coulter, Brea, CA, USA). Results were analysed using FlowJo software (FlowJo, Ashland, OR, USA).

AE1 transport in mIMCD-3 cells

mIMCD-3 cells expressing either kAE1 WT, R589H, or WT and R589H mutant were grown on glass coverslips to 70 % confluence. AE1 transport activity was measured using BCECF-AM (Sigma-Aldrich) as described previously (8). After washing with serum-free OptiMEM medium (Gibco/ Thermo Fisher), coverslips were incubated with 10 µM BCECF-AM (Sigma-Aldrich) for 10min at 37°C. Coverslips were then placed in fluorescence cuvettes and the cells were perfused at room temperature with: 5 mM glucose, 5 mM K^+ gluconate, 1 mM Ca^{2+} gluconate, 1 mM $MgSO_4$, 10 mM Hepes, 2.5 mM NaH_2PO_4, 25 mM $NaHCO_3$, 140 mM chloride, followed by a chloride-free medium containing 140 mM gluconate to induce intracellular alkalization. Solutions were continuously bubbled with 5 % CO_2. Using a PTI fluorimeter (Photon Technologies International (PTI), Edison, NJ, USA), fluorescence was excited at 440 and 490 nm, and fluorescence emission was recorded at 510 nm. Intracellular BCECF fluorescence was calibrated with buffers at pH values of 6.5, 7.0, or 7.5, each containing 100 µM nigericin sodium salt. Cellular anion exchange rates were determined by linear regression of the initial 60 s of fluorescence perturbation, and normalized to pH calibration measurements, using FelixGX 4.1.0 software (PTI). Results represent $\geq$ 3 independent experiments.

Reverse transcription and quantitative PCR

Total RNA (2 µg from renal cortex or medulla; 5 µg from liver) was reverse-transcribed with SuperScript III Reverse Transcriptase (Invitrogen Life Technologies, Carlsbad, CA, USA) as described previously (9). Duplicate qPCR reactions were perfomed with SsoFast EvaGreen Supermix (BioRad, Hercules, CA, USA) using a CFX96 Touch Real-Time PCR Cycler (BioRad). Primer sequences were "flAe1_for"

(5'-CCCCATACACCATCCTCTC-3', "flAe1_rev" (5'-CGGTTATGCGCCATGGA-3'), and the ActB Quantitect Primer Assay QT01136772 (Qiagen, Hilden, Germany).

Antibodies

Primary antibodies use in this study: rabbit anti-NBCn1 (Kwon et al. AJP 282: F341-F351, 2002; PMID 11788449) (Western Blot 1:5000; Immunofluorescence 1:2500); rabbit anti-rkNBC1 (not clear) (WB 1:5000); rabbit anti-NHE3 (Catalog number SPC-400, StressMarq Biosciences, Victoria, BC, Canada); rabbit anti-AE2 (Frische AJP renal 2004 PMID 14749257) (WB 1:3000); rabbit anti-pendrin (10) (WB 1:10000); rabbit anti-Atp6v1b1 subunit (11) (WB 1:30,000); chicken anti-Atp6v1e1 subunit (12) (IF 1:500); rabbit anti-Atp6v0a4 subunit (6) (1:500); guinea pig anti-AE1 (6) (IF 1:5000); guinea pig anti-pendrin (6) (IF 1:1000); goat anti-AQP2 (C-17; Santa Cruz, Dallas, TX, USA) (IF 1:1000); sheep anti-CA2 (AHP206; Serotec, Kidlington, UK) (IF 1:500); anti-Diego b (1:4) human monoclonal antibodies were kindly donated by Dr. M. Uchikawa, Japanese Red Cross Central Blood Center, Tokyo; mouse anti-HA (Covance, Princeton, NJ, USA) (IF 1:500 and WB 1:1500); mouse anti-myc (Cell Signalling, Danvers, MA, USA) (IF 1:500 and WB 1:1500).

Secondary antibodies used in this study: goat anti-rabbit Alexa 555 (Invitrogen, Carlsbad, CA, USA) (1:2000); goat anti-rabbit Alexa 488 (Invitrogen) (1:2000); goat anti guinea pig Alexa 555 (Invitrogen) (1:2000); goat anti guinea pig Alexa 488 (Invitrogen) (1:2000), anti-mouse coupled to HRP (Cell signalling, Danvers, MA, USA) (WB 1:10000), anti-rabbit coupled to HRP (Cell signalling, Danvers, MA, USA) (WB 1:10000).

Cell surface measurements

The cell surface of type A intercalated cells (basolateral AE1 and apical B1 subunit localization) was determined in the inner stripe of the outer medulla with ImageJ. Briefly, a grid of arbitrary size was placed on immunohistochemistry pictures and the stained cell area within each grid was calculated as a ratio of unit grid. To avoid biased measurements of type A intercalated cells 5 different randomly selected grid sizes were applied and the mean calculated (13). In total, type A intercalated cells of 2 different mice per genotype were measured. Cortical type A intercalated cells were

not measured due to weak staining in heterozygous and homozygous Ae1-R607H knock-in mice.

Statistics

The three genotype groups were compared by one-way ANOVA followed by Tukey's multiple comparisons test. P-value < 0.05 was considered significant.

Supplementary Figures

Supplementary Figure 1. (A) Targeting and screening strategy. Top: murine *Ae1* locus; middle: targeted locus; lower: locus after Cre-mediated removal of the selection cassette. (**B**) Clones were screened by Southern blot using *Hind*III and an external probe as indicated. The probe detected a 20 kb WT fragment and a 4.8 kb targeted fragment. (**C**) Histological analysis of mouse kidney sections at 3 months of age revealed no abnormalities (Masson Goldner, scale bar 50 µm). (**D**) Von Kossa stain revealed no detectable nephrocalcinosis (scale bar 50 µm).

Supplementary Figure 2. (**A-G**) After 3 days under standard conditions to determine baseline values, $Ae1^{+/+}$ (n=6; diamond), $Ae1^{+/R607H}$ (n=10; square) and $Ae1^{R607H/R607H}$ (n=8; triangle) mice were acid-challenged for 6 days with 0.28 M NH_4Cl in drinking water. (A) Blood [HCO_3^-]. (B) Blood pCO_2. (C) Urinary net acid excretion (NAE). (D) Urinary titrable acid (TA). (E) Body weight. (F) Water intake. (G) Food intake. Data are presented as mean ± SEM. $^{*}P<0.05$, $^{**}P<0.01$, $^{***}P<0.001$, $^{****}P<0.0001$ indicated for $Ae1^{+/R607H}$ or $Ae1^{R607H/R607H}$ vs. $Ae1^{+/+}$, other data points not significant, $Ae1^{+/R607H}$ vs. $Ae1^{R607H/R607H}$ no significant difference at any time point (Two-way ANOVA).

Supplementary Figure 3. Grey scaled images of the immunofluorescence stainings displayed in Figure 3. Scale bars: 10 µm.

Supplementary Figure 4. (**A**) Coomassie blue stained gel of RBC lysates from WT (n=4), $Ae1^{+/R607H}$ (n=5), and $Ae1^{R607H/R607H}$ (n=5) mice (**B**) Quantification of Ae1 protein expression normalized to actin. No significant differences between genotypes.

Supplementary Figure 5. Representative western blots for Ae1 protein abundance in protein lysates from cortex (**A**) and medulla (**B**) of WT, $Ae1^{+/R607H}$ and $Ae1^{R607H/R607}$ mice.

Supplementary Figure 6. Representative western blot for pulse-chase experiments. (**A**) M1 cells transfected with human kAE1-WT. (**B**) M1 cells transfected with human

kAE1-R589H. (**C**) mIMCD-3 cells transfected with human kAE1-WT. (**D**) mIMCD-3 cells transfected with human kAE1-R589H. Unfilled circles indicate non-glycosylated protein; filled circles indicate glycosylated protein.

Supplementary Figure 7. Merged channels (**A-C**) for co-immunostainings for the Ae1 (**D-F**) and the B1 subunit of the V-type ATPase (**G-I**) in inner stripe of outer medulla under baseline conditions. Single channels for Ae1. (**G-I**) Single channel for B1. Scale bars: 10 µm.

Supplementary Figure 8. Merged channels (**A-C**) for co-immunostainings for the Ae1 (**D-F**) and the B1 subunit of the V-type ATPase (**G-I**) in inner stripe of outer medulla under acid challenge. Single channels for Ae1. (**G-I**) Single channel for B1. Scale bars: 10 µm.

Supplementary Figure 9. Immunogold labelling of the A subunit of the V-type ATPase in type B intercalated cells in the cortex. (**A-C**) Overview from WT, *Ae1*$^{+/R607H}$ and *Ae1*$^{R607H/R607H}$ mice. Scale bar: 2 µm. (**D-F**) Magnification of the basolateral cell pole. Scale bar: 1 µm (**G-I**) Magnification of the apical cell pole. Scale bar: 1 µm. (**J**) Pendrin protein abundance analyzed in whole kidney protein lysates is unchanged in *Ae1*$^{+/R607H}$ and *Ae1*$^{R607H/R607}$ mice compared to wild-type mice. Data are presented as means ± SEM; n=5 for wild-type and *Ae1*$^{+/R607H}$, n=4 *Ae1*$^{R607H/R607H}$ mice.

Supplementary Figure 10. (**A-C**) Renal cortex showing merged channels of the co-staining for Ae1 (red), Pendrin (blue), and the E-subunit (green) of the V-type ATPase. (**D-F**) Single channels for Ae1. (**G-I**) Single channels for the E subunit. (**J-L**) Single channels for Pendrin. Scale bars: 25 µm.

Supplementary Figure 11. (**A-C**) Renal cortex showing merged channels of the co-staining for Ae1 (red), Pendrin (blue), and Aquaporin 2 (green). (**D-F**) Single channels for Ae1. (**G-I**) Single channels for Aquaporin 2. (**J-L**) Single channels for Pendrin. Scale bars: 25 µm.

Supplementary Figure 12. (**A-C**) Renal cortex showing merged channels of the co-staining for Ae1 (red), p62 (green), and DAPI (blue). (**D-F**) Single channels for Ae1. (**G-I**) Single channels for p62. (**J-L**) Single channels for DAPI. Scale bars: 25 µm.

Supplementary Figure 13. (**A-C**) Renal medulla showing merged channels of the co-staining for Ae1 (red), p62 (green), and DAPI (blue). (**D-F**) Single channels for Ae1. (**G-I**) Single channels for p62. (**J-L**) Single channels for DAPI. Scale bars: 25 µm.

Supplementary Figure 14. (**A-C**) Renal cortex showing merged channels of the co-staining for Ubiquitin (red), p62 (green), and DAPI (blue). (**D-F**) Single channels for Ubiquitin. (**G-I**) Single channels for p62. (**J-L**) Single channels for DAPI. Scale bars: 10 µm.

Supplementary References

1. Schwenk F, Baron U, and Rajewsky K. A cre-transgenic mouse strain for the ubiquitous deletion of loxP-flanked gene segments including deletion in germ cells. *Nucleic acids research.* 1995;23(24):5080-1.
2. Hennings JC, Picard N, Huebner AK, Stauber T, Maier H, Brown D, Jentsch TJ, Vargas-Poussou R, Eladari D, and Hubner CA. A mouse model for distal renal tubular acidosis reveals a previously unrecognized role of the V-ATPase a4 subunit in the proximal tubule. *EMBO molecular medicine.* 2012;4(10):1057-71.
3. Sinning A, Liebmann L, Kougioumtzes A, Westermann M, Bruehl C, and Hubner CA. Synaptic glutamate release is modulated by the Na+ -driven Cl-/HCO(3)(-) exchanger Slc4a8. *The Journal of neuroscience : the official journal of the Society for Neuroscience.* 2011;31(20):7300-11.
4. Cordat E, Kittanakom S, Yenchitsomanus PT, Li J, Du K, Lukacs GL, and Reithmeier RA. Dominant and recessive distal renal tubular acidosis mutations of kidney anion exchanger 1 induce distinct trafficking defects in MDCK cells. *Traffic.* 2006;7(2):117-28.
5. Paunescu TG, Ljubojevic M, Russo LM, Winter C, McLaughlin MM, Wagner CA, Breton S, and Brown D. cAMP stimulates apical V-ATPase accumulation, microvillar elongation, and proton extrusion in kidney collecting duct A-intercalated cells. *American journal of physiology Renal physiology.* 2010;298(3):F643-54.
6. Stehberger PA, Shmukler BE, Stuart-Tilley AK, Peters LL, Alper SL, and Wagner CA. Distal renal tubular acidosis in mice lacking the AE1 (band3) Cl-/HCO3-exchanger (slc4a1). *Journal of the American Society of Nephrology : JASN.* 2007;18(5):1408-18.

7. Frumence E, Genetet S, Ripoche P, Iolascon A, Andolfo I, Le Van Kim C, Colin Y, Mouro-Chanteloup I, and Lopez C. Rapid Cl(-)/HCO(-)(3)exchange kinetics of AE1 in HEK293 cells and hereditary stomatocytosis red blood cells. *American journal of physiology Cell physiology.* 2013;305(6):C654-62.
8. Sterling D, and Casey JR. Transport activity of AE3 chloride/bicarbonate anion-exchange proteins and their regulation by intracellular pH. *The Biochemical journal.* 1999;344 Pt 1(221-9.
9. Rust MB, Faulhaber J, Budack MK, Pfeffer C, Maritzen T, Didie M, Beck FX, Boettger T, Schubert R, Ehmke H, et al. Neurogenic mechanisms contribute to hypertension in mice with disruption of the K-Cl cotransporter KCC3. *Circulation research.* 2006;98(4):549-56.
10. Knauf F, Yang CL, Thomson RB, Mentone SA, Giebisch G, and Aronson PS. Identification of a chloride-formate exchanger expressed on the brush border membrane of renal proximal tubule cells. *Proceedings of the National Academy of Sciences of the United States of America.* 2001;98(16):9425-30.
11. Vallet M, Picard N, Loffing-Cueni D, Fysekidis M, Bloch-Faure M, Deschenes G, Breton S, Meneton P, Loffing J, Aronson PS, et al. Pendrin regulation in mouse kidney primarily is chloride-dependent. *Journal of the American Society of Nephrology : JASN.* 2006;17(8):2153-63.
12. Breton S, Wiederhold T, Marshansky V, Nsumu NN, Ramesh V, and Brown D. The B1 subunit of the H+ATPase is a PDZ domain-binding protein. Colocalization with NHE-RF in renal B-intercalated cells. *The Journal of biological chemistry.* 2000;275(24):18219-24.
13. West MJ. Estimating volume in biological structures. *Cold Spring Harbor protocols.* 2012;2012(11):1129-39.

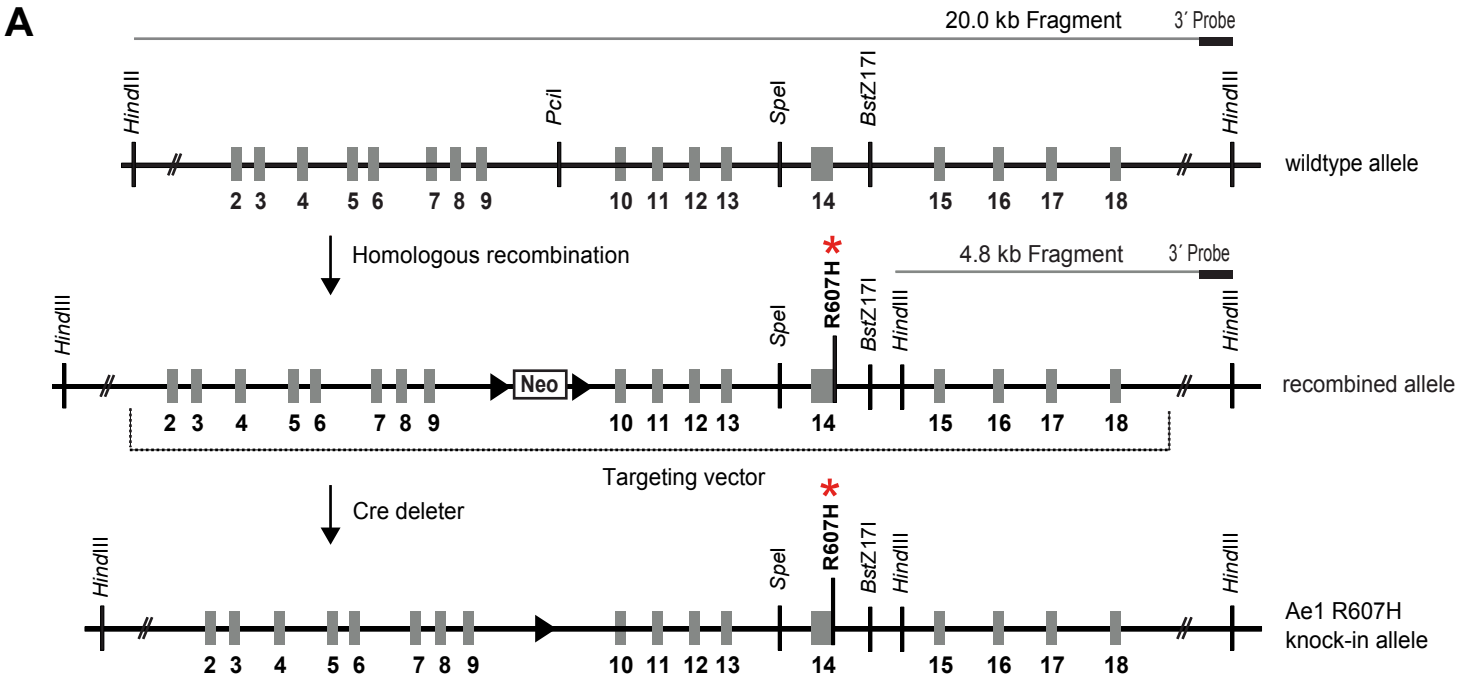

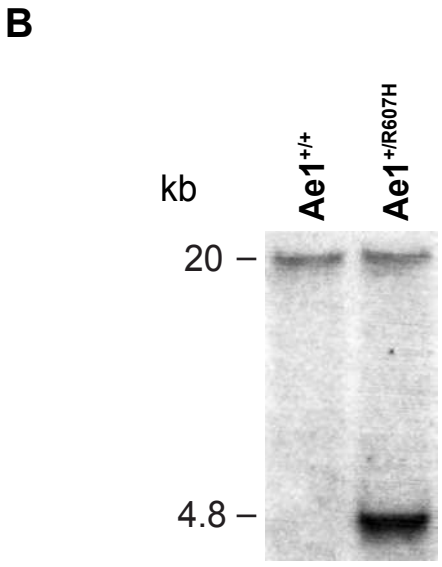

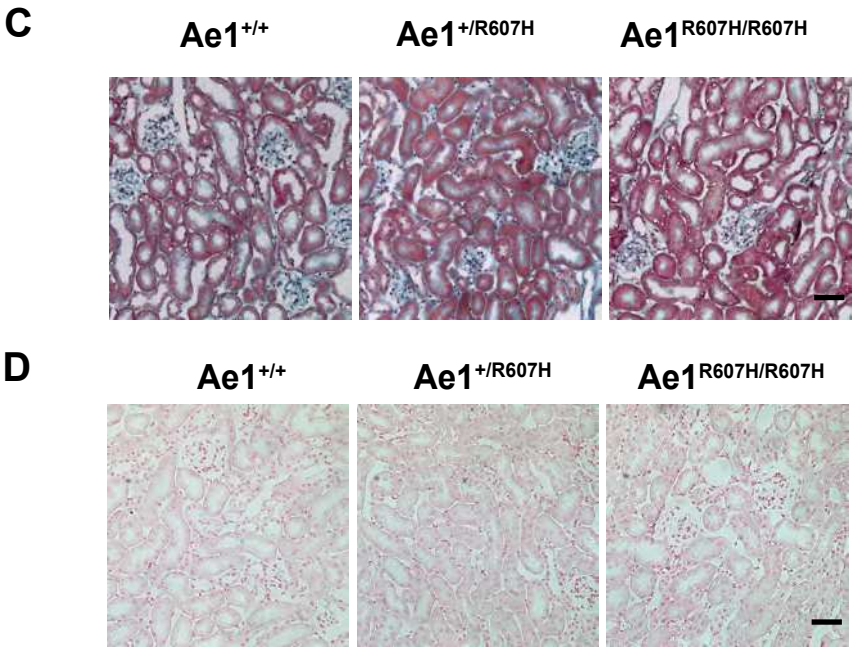

Supplementary Figure: 1

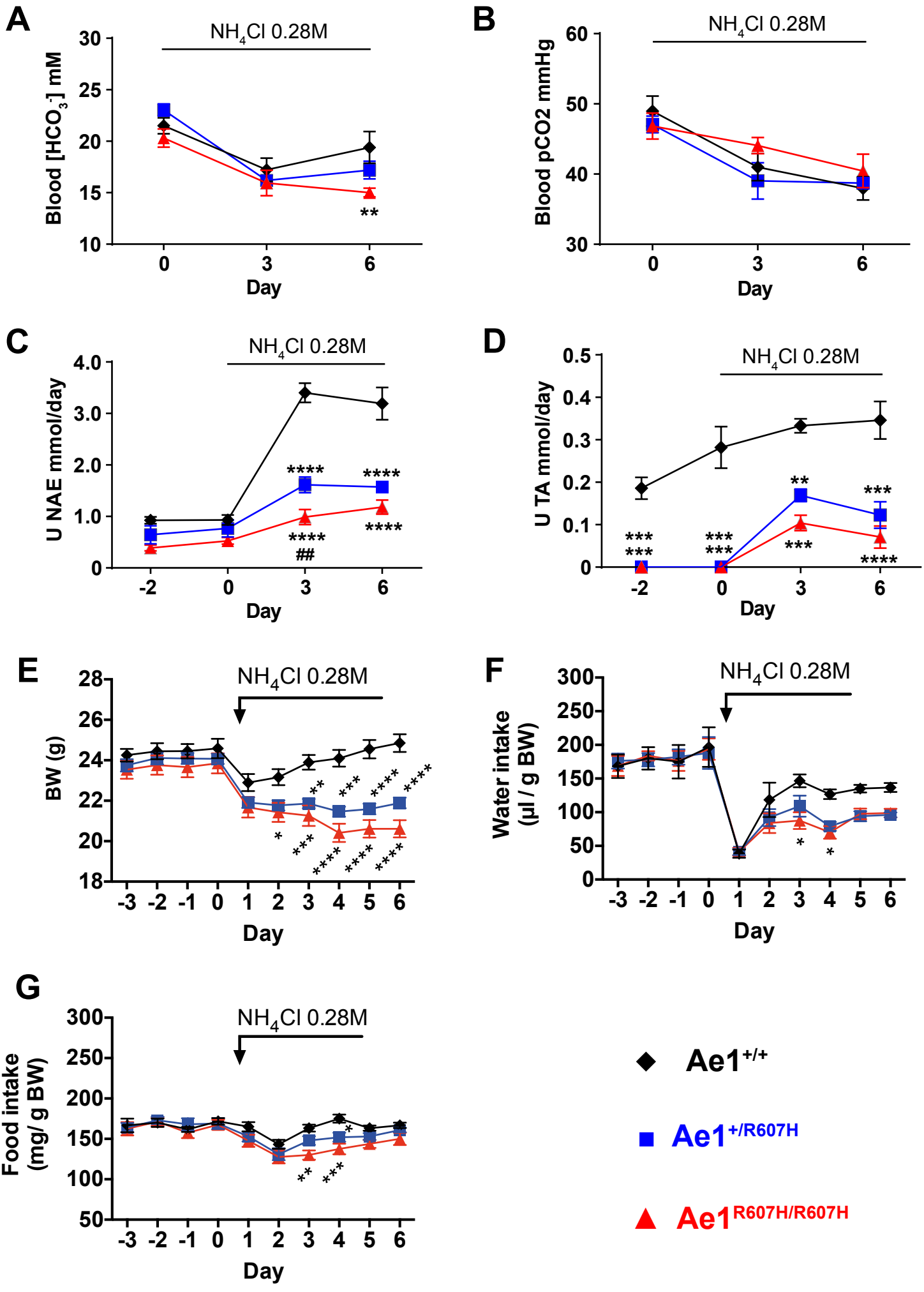

Supplementary Figure: 2

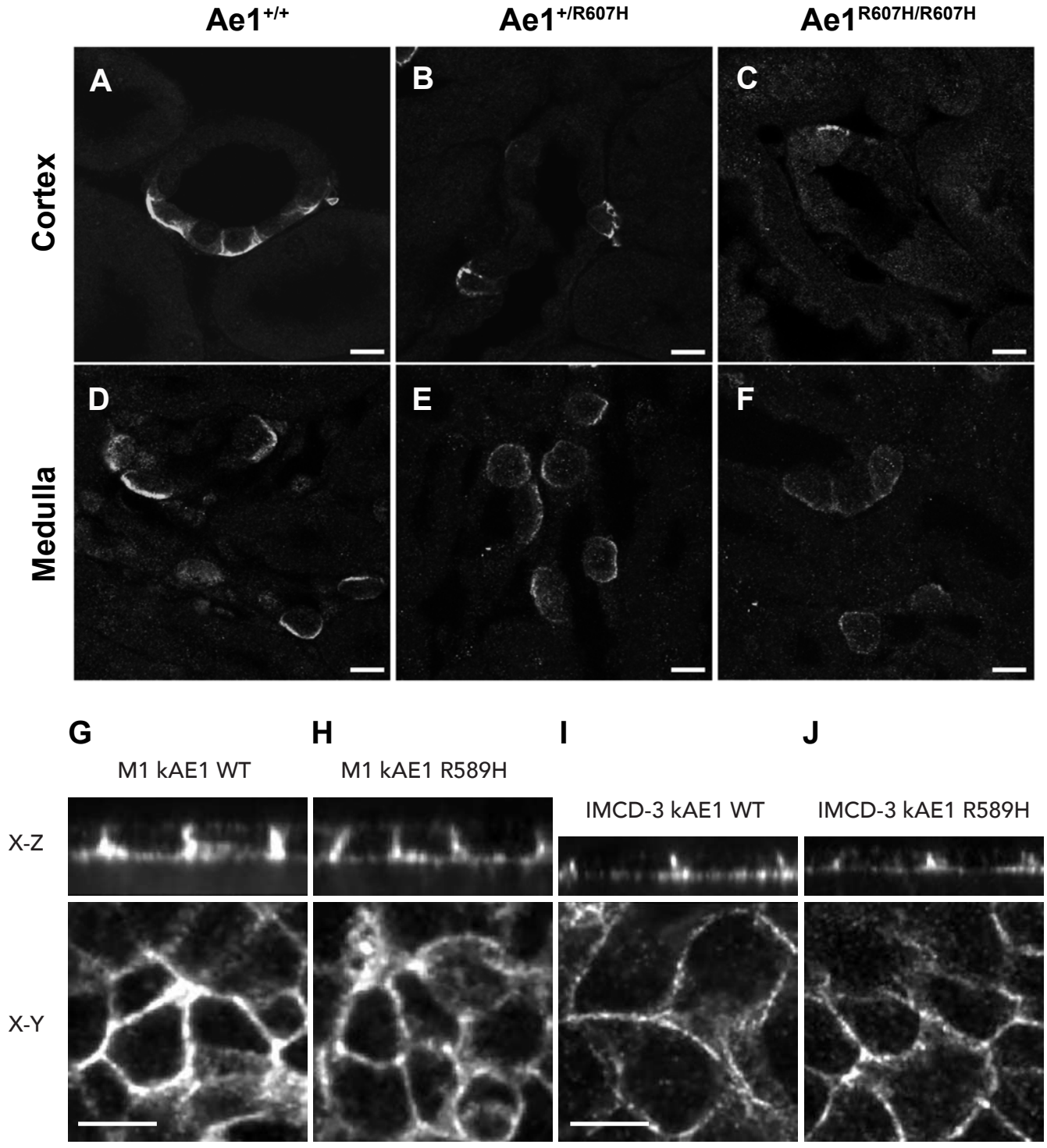

Supplementary Figure: 3

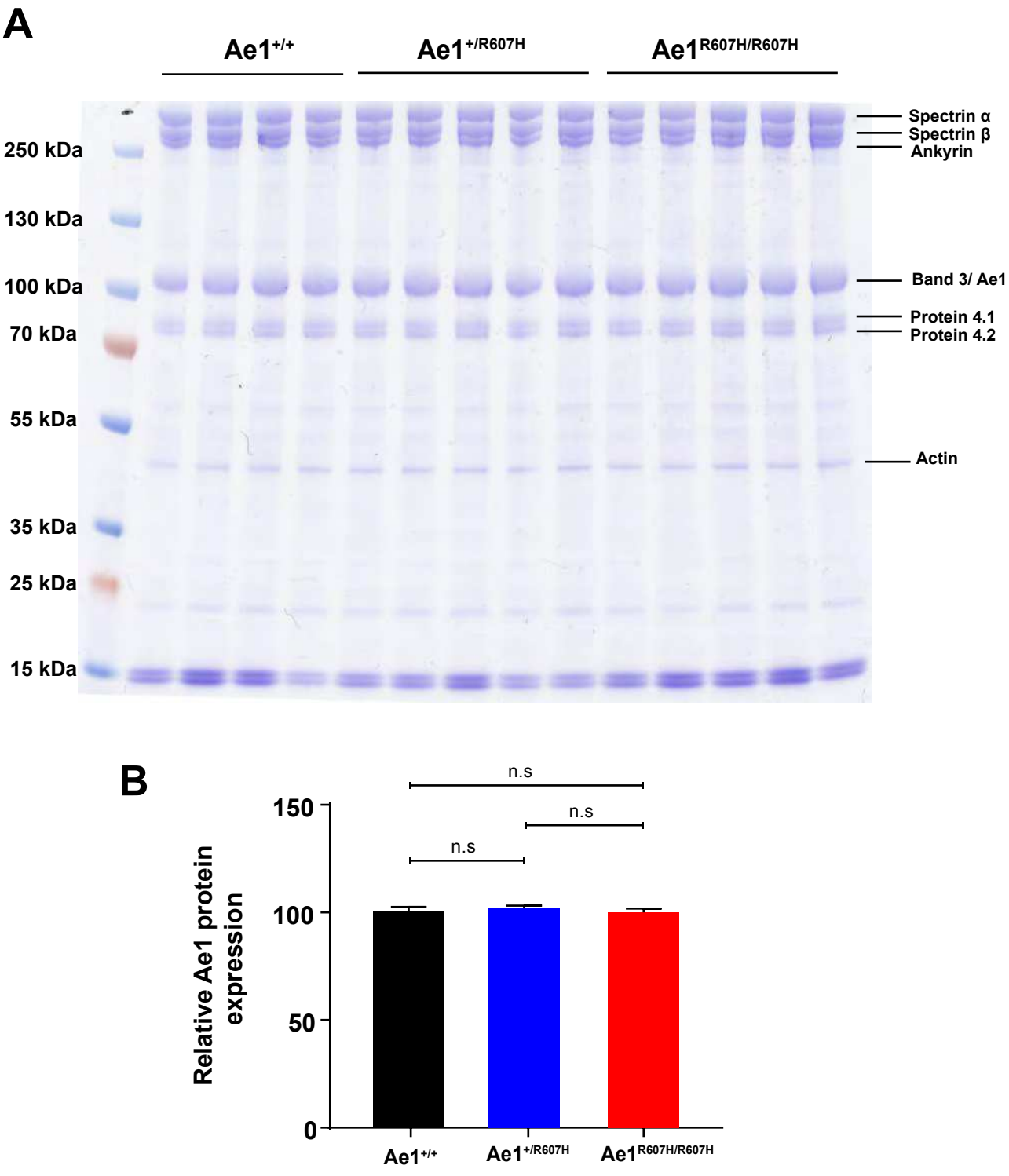

Supplementary Figure: 4

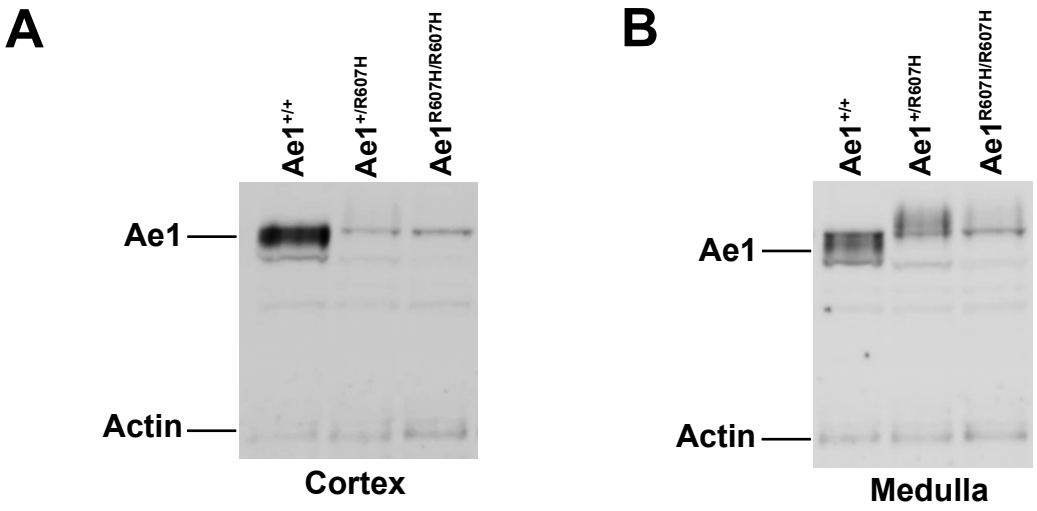

Supplementary Figure: 5

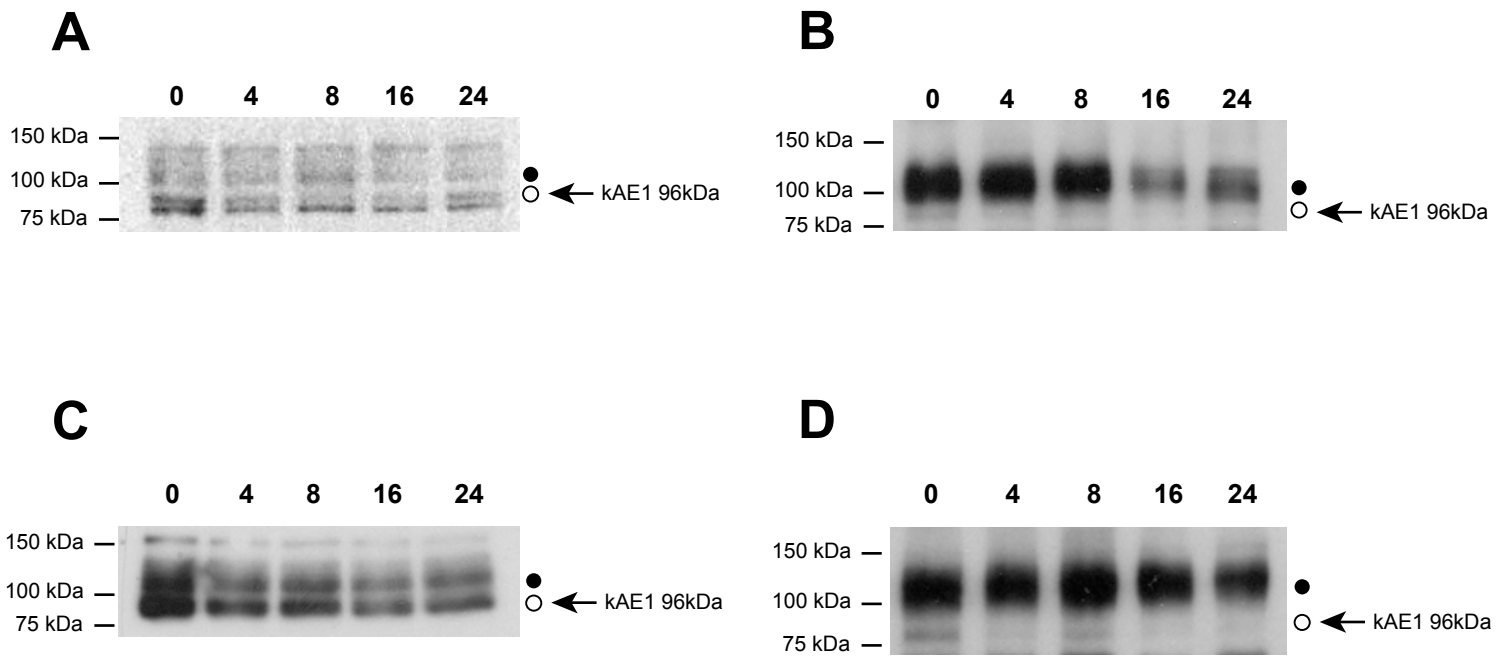

Supplementary Figure: 6

A M1 AE1-WT
B M1 AE1-R589H
C mIMCD3 AE1-WT
D mIMCD3 AE1-R589H

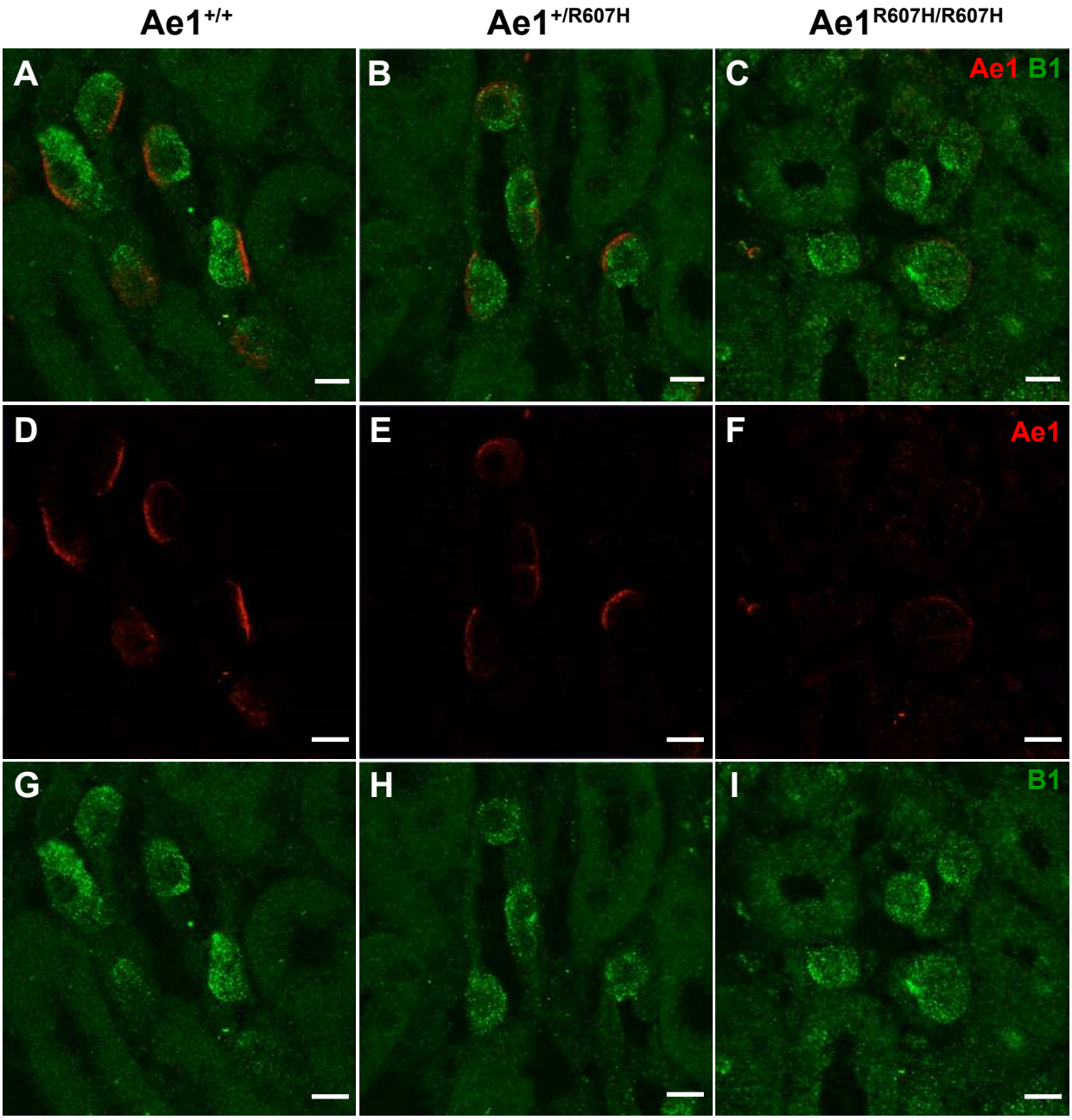

Supplementary Figure: 7

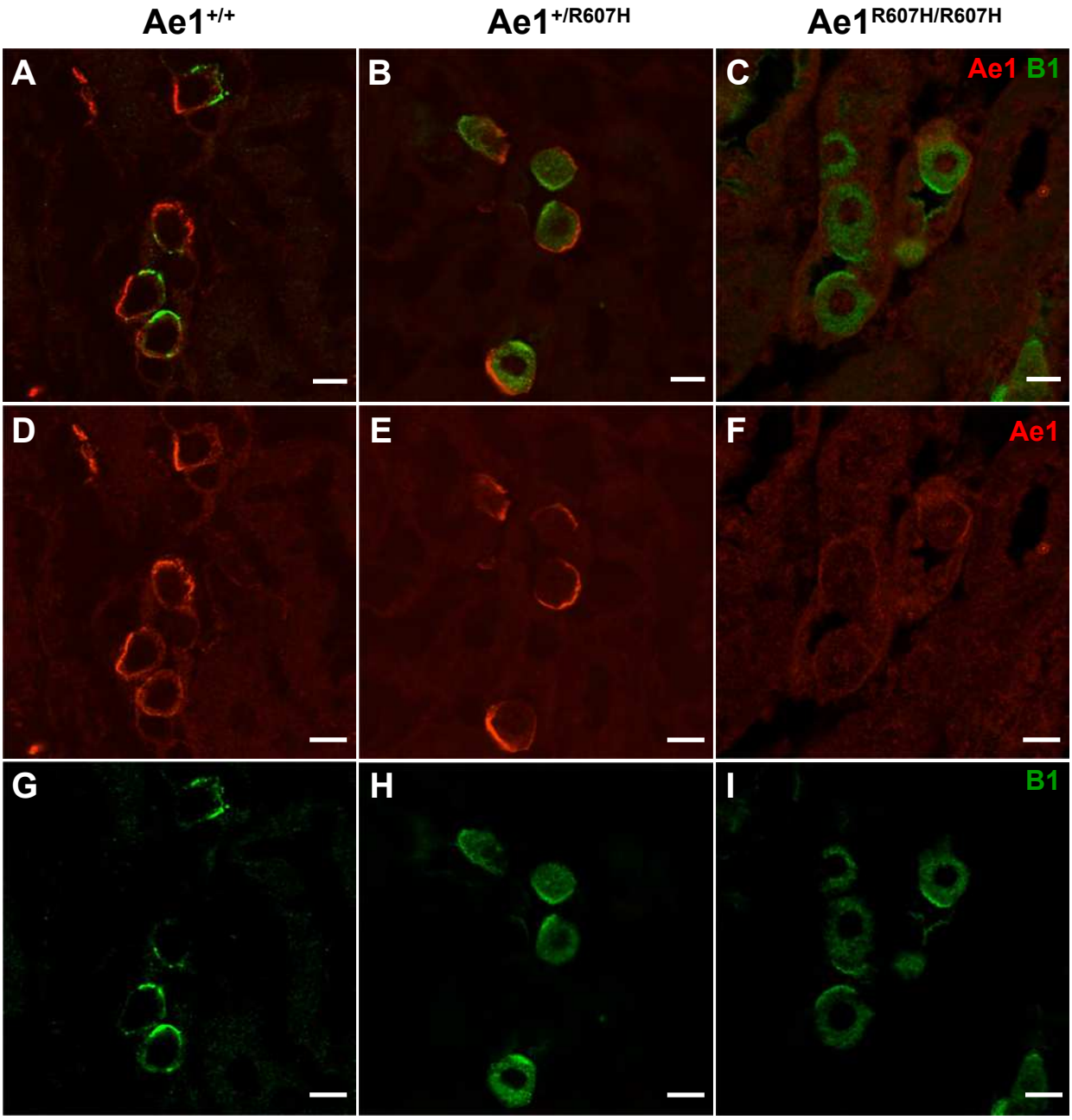

Supplementary Figure: 8

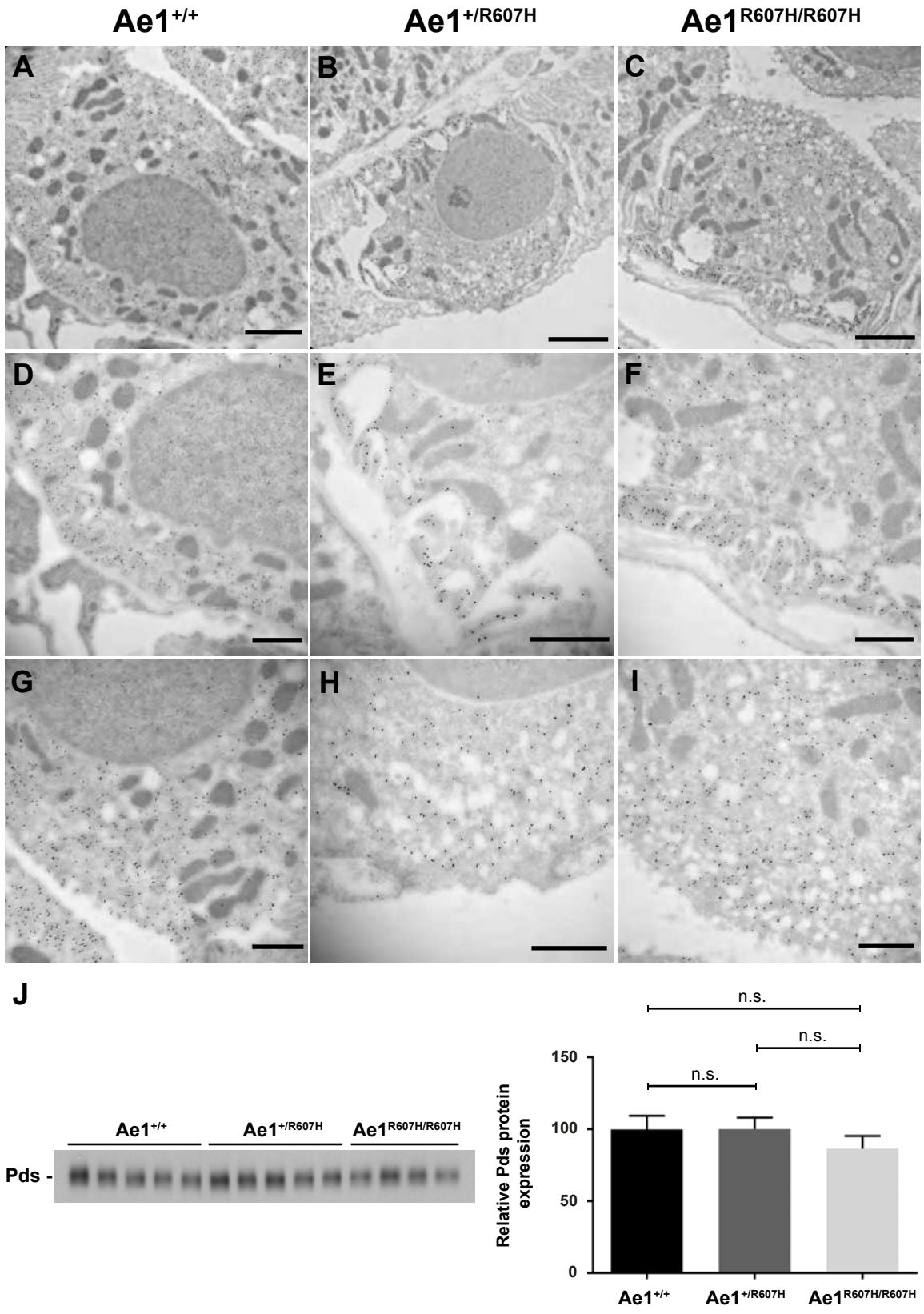

Supplementary Figure: 9

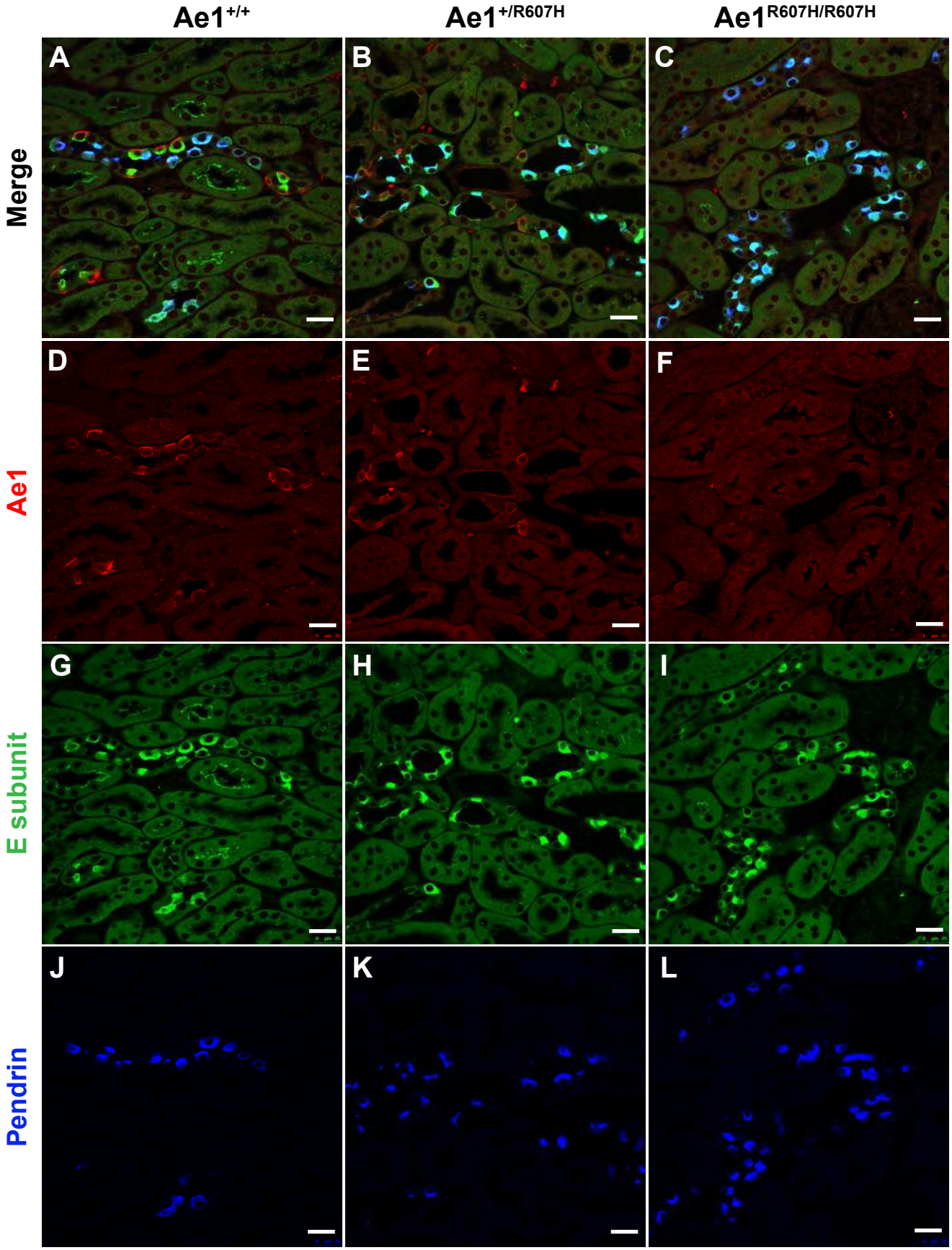

Supplementary Figure: 10

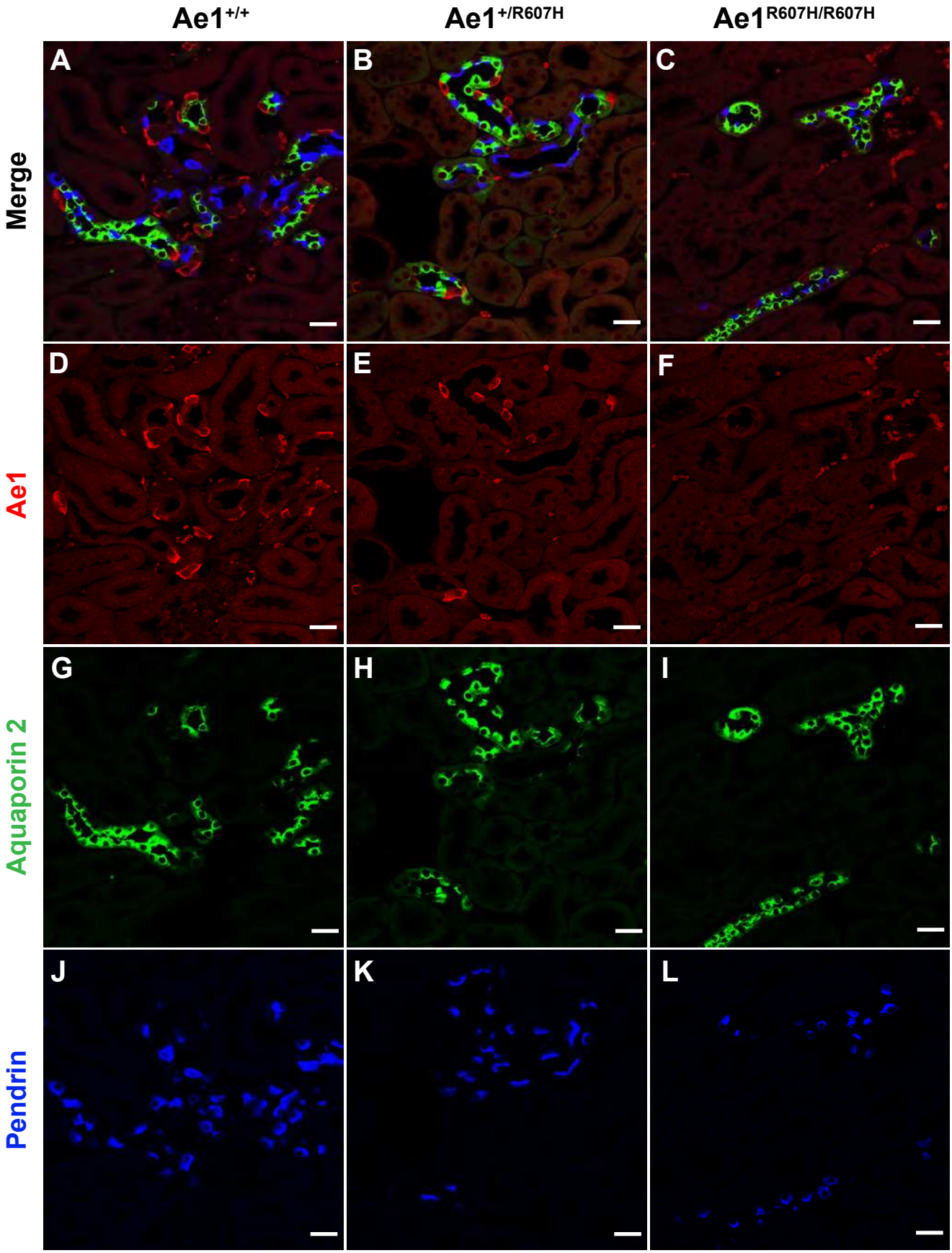

Supplementary Figure: 11

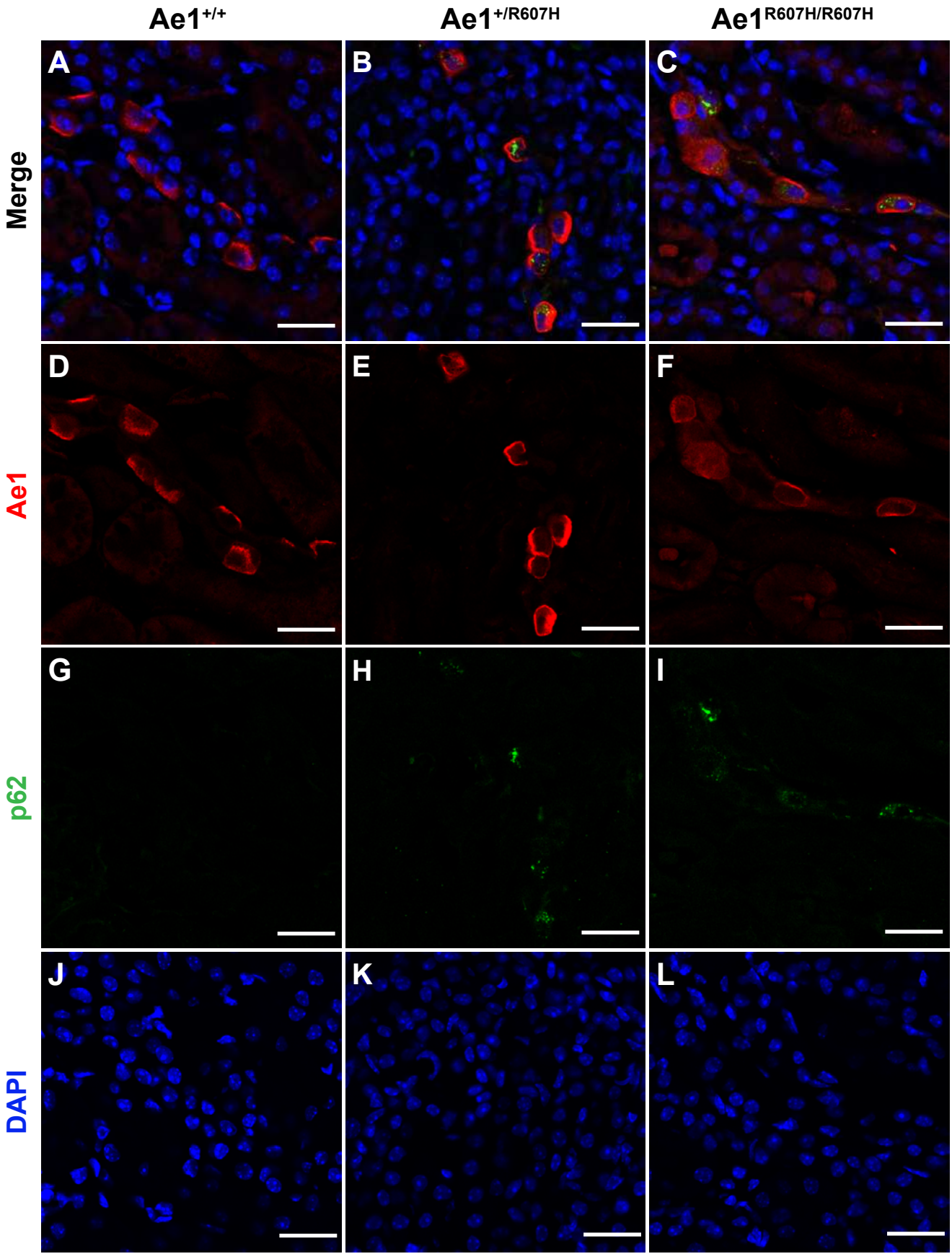

Supplementary Figure: 12

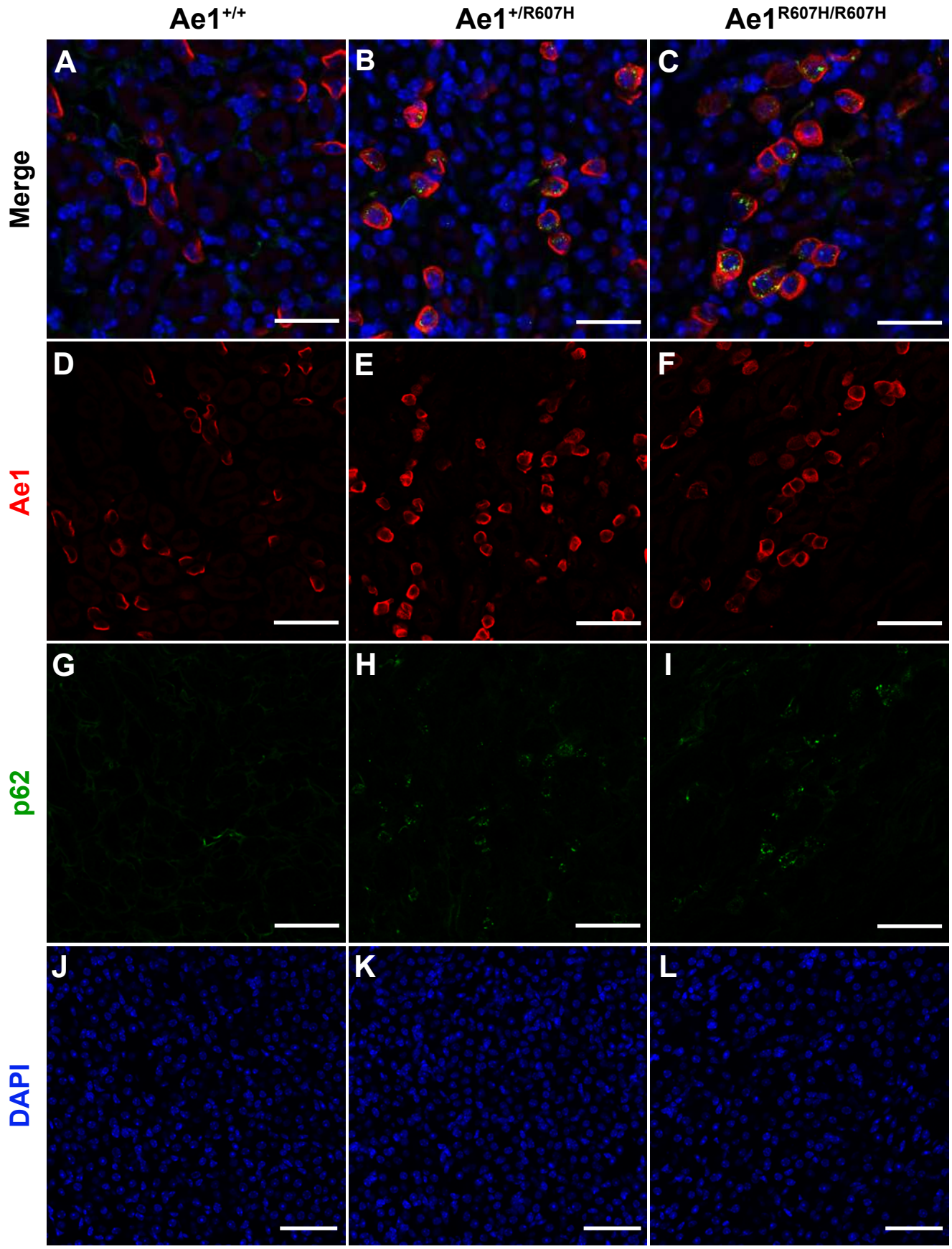

Supplementary Figure: 13

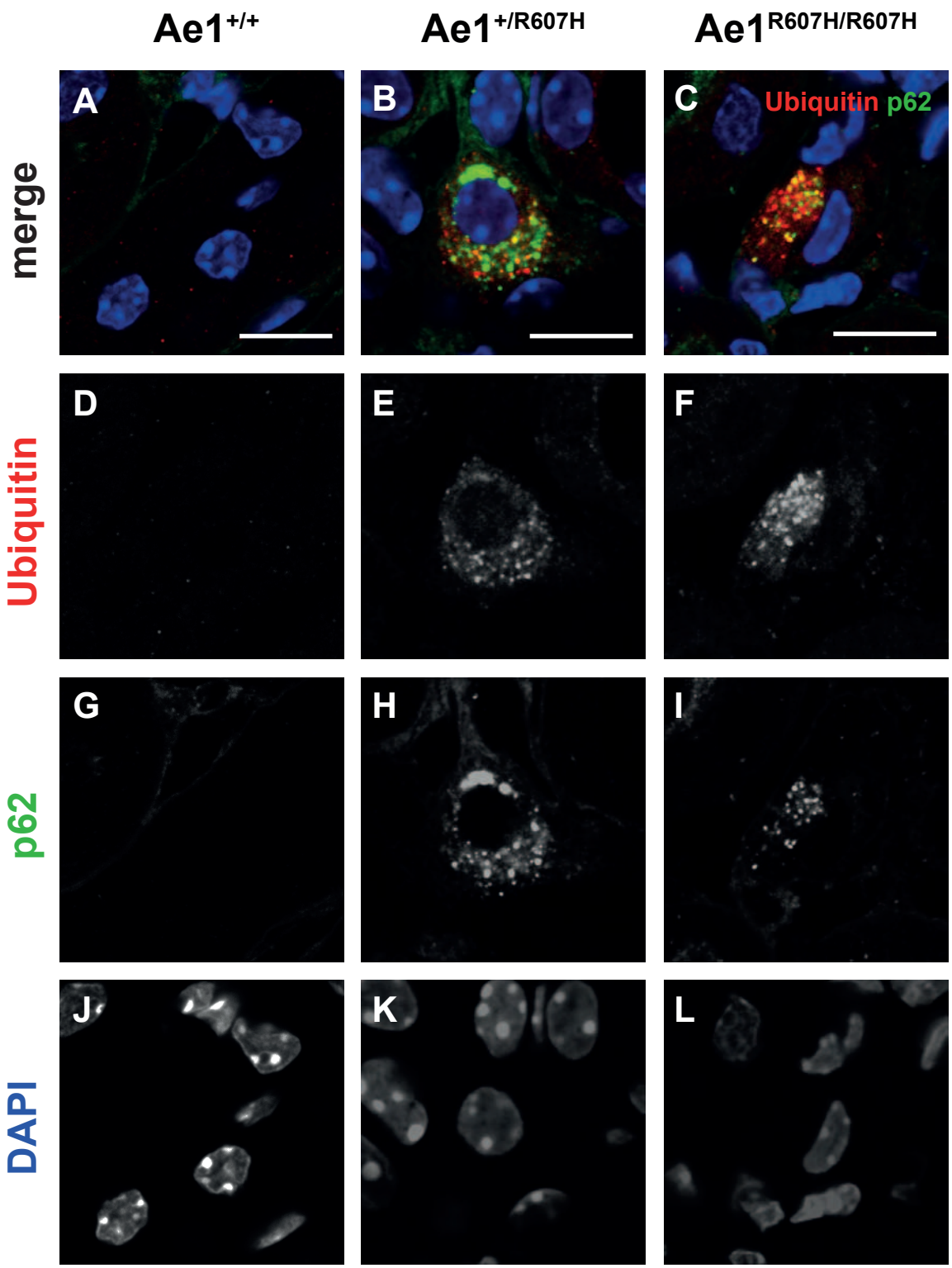

Supplementary Figure: 14